



## RESEARCH ARTICLE SUMMARY

## CANCER IMMUNOTHERAPY

# A microbiota-modulated checkpoint directs immunosuppressive intestinal T cells into cancers

Marine Fidelle *et al.*

**INTRODUCTION:** Resistance of cancers to immune checkpoint inhibitors (ICIs) can result from antibiotic (ABX) treatment, likely as a result of a deviated gut microbiota. ABX compromise clinical outcome when administered before, rather than during, ICI administration, suggesting that bacterial recolonization following ABX discontinuation may be deleterious. Gut commensals induce the differentiation of an immunosuppressive subset of FoxP3<sup>+</sup> retinoic acid receptor-related orphan receptor- $\gamma$ t (ROR $\gamma$ t<sup>+</sup>) regulatory (T<sub>reg</sub>) cells. Lymphocytes primed in the mesenteric lymph nodes (mLNs) or homing to the intestinal lamina propria express the  $\alpha$ 4 $\beta$ 7 integrin interacting with its counter-receptor, mucosal addressin cell adhesion molecule-1 (MAdCAM-1), which is expressed in high endothelial venules (HEVs).

**RATIONALE:** We hypothesized that disruption of the MAdCAM-1- $\alpha$ 4 $\beta$ 7 interaction that retains T<sub>reg</sub> cells might cause their migration from the gut to tumors and thereby compromise the anticancer effects of ICIs. We used two complementary methods to visualize the exodus of

intestinal T cells to subcutaneous tumors and tumor-draining lymph nodes (tdLNs): (i) Kaede mice expressing a fluorescent protein that is photoconverted upon ultraviolet light illumination of the ileum and (ii) the injection of carboxyfluorescein succinimidyl ester into mLNs. Moreover, we used transgene-enforced *Madcam1* expression in the liver to locally intercept T<sub>reg</sub> cells during their migration.

**RESULTS:** Several classes of ABX down-regulated *Madcam1* expression in ileal venules, Peyer's patches and mLNs, coinciding with the ileal exodus of  $\alpha$ 4 $\beta$ 7<sup>+</sup> T helper (T<sub>H</sub>17) and T<sub>reg</sub> cells toward extraintestinal tumors and tdLNs. This ABX-induced reduction in MAdCAM-1 could be explained by the recolonization of the gut by the genus *Enterocloster* (encompassing the *E. clostridioformis* species), because its oral administration was sufficient to down-regulate MAdCAM-1 expression through its effects on bile acid metabolism. Genetic or antibody-mediated neutralization of MAdCAM-1 or  $\alpha$ 4 $\beta$ 7 integrin phenocopied the immunosuppressive effects of ABX, promoting resistance to ICIs targeting programmed cell death protein 1 (PD-1)

and inducing a surge in gut-derived  $\alpha$ 4 $\beta$ 7<sup>+</sup> T<sub>reg</sub> cells in tdLNs and tumors. Restoration of MAdCAM-1 on ileal HEV by fecal microbial transplantation or blockade of IL-17A reversed the inhibitory effects of ABX. Ectopic expression of MAdCAM-1 in the liver caused the local retention of enterotropic  $\alpha$ 4 $\beta$ 7<sup>+</sup> T<sub>reg</sub> cells, reducing their accumulation in tumor beds and improving immunotherapy outcomes in mice. Finally, low-serum-soluble MAdCAM-1 was identified as a proxy of intestinal dysbiosis and a robust predictor of shorter overall and progression-free survival of renal, bladder, and lung cancer patients under immunotherapy with antibodies targeting PD-1 or PD-L1. In non-small-cell lung cancer patients, the prognostic value of soluble MAdCAM-1 was independent of PD-L1 expression.

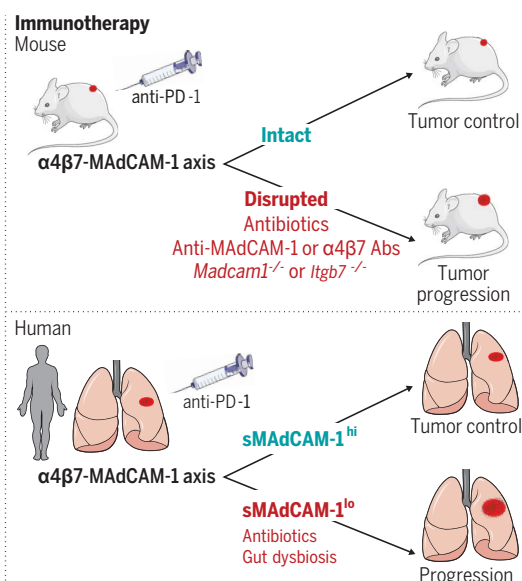
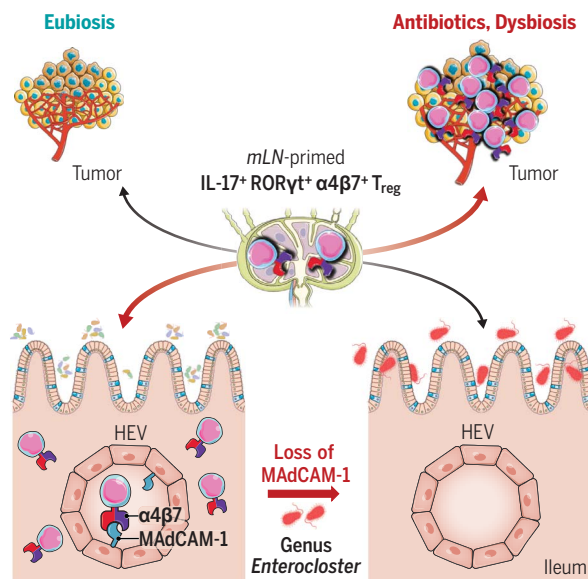
**CONCLUSION:** The relocation of enterotropic and immunosuppressive T<sub>reg</sub> cells to cancerous tissue (tumors and tdLNs) is repressed by the molecular interaction between the HEV addressin MAdCAM-1 and the integrin  $\alpha$ 4 $\beta$ 7 expressed by T<sub>reg</sub> cells. Disruption of the MAdCAM-1 expression by ABX or gut dysbiosis causes the relocation of T<sub>reg</sub> cells into tumors, consequently compromising cancer immunosurveillance and the therapeutic efficiency of ICIs in mice and patients. ■

The complete list of authors and their affiliations is available in the full article online.

Corresponding author. Email: Laurence Zitvogel, laurence.zitvogel@gustaveroussy.fr; Guido Kroemer, kroemer@orange.fr; Conrad Rauber, conrad.rauber@gmx.de  
Cite this article as M. Fidelle *et al.*, *Science* **380**, eabo2296 (2023). DOI: 10.1126/science.abo2296

**READ THE FULL ARTICLE AT**  
<https://doi.org/10.1126/science.abo2296>

**MAdCAM-1 as a gut immune checkpoint for cancer immunosurveillance.** Bacteria from the genus *Enterocloster*, for example, after discontinuation of ABX, induce the down-regulation of MAdCAM-1 in the ileal lamina propria and mLNs, inducing the exodus of the immunosuppressive  $\alpha$ 4 $\beta$ 7<sup>+</sup> T<sub>reg</sub> cells from the gut to cancers and tdLNs. Disruption of the MAdCAM-1- $\alpha$ 4 $\beta$ 7 axis compromises the efficacy of immunotherapy in mice and patients.



## RESEARCH ARTICLE

## CANCER IMMUNOTHERAPY

# A microbiota-modulated checkpoint directs immunosuppressive intestinal T cells into cancers

Marine Fidelle<sup>1,2,3,†</sup>, Conrad Rauber<sup>1,2,3,4,\*†</sup>, Carolina Alves Costa Silva<sup>1,2,3,†</sup>, Ai-Ling Tian<sup>1,2, 5, 6</sup>, Imran Lahmar<sup>1,2,3</sup>, Anne-Laure Mallard de La Varende<sup>1,2,3</sup>, Liwei Zhao<sup>1,5,6</sup>, Cassandra Thelemaque<sup>1,3</sup>, Isabelle Lebhar<sup>1,3</sup>, Meriem Messaoudene<sup>7</sup>, Eugénie Pizzato<sup>1,3</sup>, Roxanne Birebent<sup>1,2,3</sup>, Maxime Descartes Mbogning Fonkou<sup>1,3</sup>, Silvia Zoppi<sup>1,2,8</sup>, Anna Reni<sup>1,2,9</sup>, Cécile Dalban<sup>10</sup>, Marion Leduc<sup>1,5,6</sup>, Gladys Ferrere<sup>1,3,11</sup>, Sylvère Durand<sup>1,5,6</sup>, Pierre Ly<sup>1,3,12</sup>, Aymeric Silvain<sup>1,3</sup>, Kevin Mulder<sup>1,2,3</sup>, Charles-Antoine Dutertre<sup>1,3</sup>, Florent Ginhoux<sup>1,3</sup>, Satoru Yonekura<sup>1,2,3</sup>, Maria Paula Roberti<sup>1,3,13,14</sup>, Maryam Tidjani-Alou<sup>1,3</sup>, Safae Terrisse<sup>1,2,3</sup>, Jianzhou Chen<sup>1,3</sup>, Oliver Kepp<sup>1,5,6</sup>, Angela Schippers<sup>15</sup>, Norbert Wagner<sup>15</sup>, Javier Suárez-Gosálvez<sup>16</sup>, Sebastian Kobold<sup>16,17</sup>, Jean-Eudes Fahrner<sup>1,2,3</sup>, Corentin Richard<sup>7</sup>, Jacques Bosq<sup>18</sup>, Leonardo Lordello<sup>1,3</sup>, Giacomo Vitali<sup>19</sup>, Nathalie Galleron<sup>19</sup>, Benoît Quinquais<sup>19</sup>, Emmanuelle Le Chatelier<sup>19</sup>, Lucas Blanchard<sup>20</sup>, Jean-Philippe Girard<sup>20</sup>, Anne Jarry<sup>21</sup>, Nadine Gervois<sup>21</sup>, Emmanuelle Godefroy<sup>21</sup>, Nathalie Labarrière<sup>21,22</sup>, Ronald Koschny<sup>4</sup>, Romain Daillère<sup>11</sup>, Benjamin Besse<sup>1,2</sup>, Caroline Truntzer<sup>23</sup>, François Ghiringhelli<sup>23</sup>, Nicolas Coatnoan<sup>24,25</sup>, Vanessa Mhanna<sup>24,25</sup>, David Klatzmann<sup>24,25</sup>, Damien Drubay<sup>1,26,27</sup>, Laurence Albiges<sup>1,2</sup>, Andrew Maltez Thomas<sup>28</sup>, Nicola Segata<sup>28,29</sup>, François-Xavier Danlos<sup>1,2,3,12,30</sup>, Aurélien Marabelle<sup>1,2,3,12,30</sup>, Bertrand Routy<sup>7,31</sup>, Lisa Derosa<sup>1,2,3,12</sup>, Guido Kroemer<sup>5,6,32,\*†</sup>, Laurence Zitvogel<sup>1,2,3,12,\*†</sup>

Antibiotics (ABX) compromise the efficacy of programmed cell death protein 1 (PD-1) blockade in cancer patients, but the mechanisms underlying their immunosuppressive effects remain unknown. By inducing the down-regulation of mucosal addressin cell adhesion molecule 1 (MAdCAM-1) in the ileum, post-ABX gut recolonization by *Enterocloster* species drove the emigration of enterotropic  $\alpha 4\beta 7^+CD4^+$  regulatory T 17 cells into the tumor. These deleterious ABX effects were mimicked by oral gavage of *Enterocloster* species, by genetic deficiency, or by antibody-mediated neutralization of MAdCAM-1 and its receptor,  $\alpha 4\beta 7$  integrin. By contrast, fecal microbiota transplantation or interleukin-17A neutralization prevented ABX-induced immunosuppression. In independent lung, kidney, and bladder cancer patient cohorts, low serum levels of soluble MAdCAM-1 had a negative prognostic impact. Thus, the MAdCAM-1- $\alpha 4\beta 7$  axis constitutes an actionable gut immune checkpoint in cancer immunosurveillance.

Immune checkpoint inhibitors (ICIs) targeting the immunosuppressive interaction between programmed cell death protein 1 (PD-1) and programmed death-ligand 1 (PD-L1) are used in the clinical management of many cancer types (1, 2). Primary resistance to ICIs has been attributed to various molecular or cellular cues (3–5). In addition,

several studies confirmed the deleterious effect of antibiotics (ABX) on clinical benefit in patients receiving ICIs (6–8). Meta-analyses have revealed that ABX uptake is more harmful on clinical outcome when administered before, rather than during, ICI administration, suggesting that bacterial recolonization after an ABX course may be particularly deleteri-

ous (9–11). How these new bacterial compositions interfere with the reprogramming of the tumor microenvironment (TME) remains a conundrum.

The  $\alpha 4$  (CD49d) and  $\beta 7$  integrin subunits interact to form the  $\alpha 4\beta 7$  heterodimer. By interacting with its counter-receptor, mucosal addressin cell adhesion molecule 1 (MAdCAM-1),  $\alpha 4\beta 7$  integrin mediates lymphocyte adhesion and diapedesis from the circulation across the vascular endothelial barrier into gut-associated secondary lymphoid tissue (GALT) or the lamina propria (LP). MAdCAM-1 is constitutively expressed in LP venules, as well as in GALT high endothelial venules, and up-regulated by inflammatory cytokines (12–14). By preventing the migration of inflammatory  $\beta 7^+$  T cells from the circulation to the gut, antibodies (Abs) targeting  $\alpha 4\beta 7$  or MAdCAM-1 reduce the severity of colitis in patients with inflammatory bowel disease (15–17).

The intestinal microbiota plays a role in maintaining the homeostatic functions of gut regulatory T ( $T_{reg}$ ) and interleukin-17 (IL-17)-producing T helper ( $T_H17$ ) cells (18, 19). Gut  $T_H17$  cells also control extra-intestinal inflammation (20–24).  $T_H17$  cells and a lineage-related FoxP3<sup>+</sup>ROR $\gamma$ <sup>+</sup> regulatory subset ( $T_{reg17}$  cells) blunt antitumor immunosurveillance during carcinogenesis (25). In humans and mice, the expression of the transcription factor retinoic acid-related orphan receptor- $\gamma$  (ROR $\gamma$ ) is characteristic of a subpopulation of tumor-infiltrating  $T_{reg}$  cells that are induced by gut commensals (26–28). Thus, we hypothesized that ABX-induced overgrowth of selected species (11, 29) might affect the trafficking of  $T_{reg}$  cells between the intestinal and tumoral compartments, thereby aggravating cancer immunosuppression and resistance to PD-1 blockade.

## ABX down-regulate MAdCAM-1 ileal expression in mice and patients

The use of a cocktail of broad-spectrum ABX [ampicillin, colistin, and streptomycin (ACS)] to sterilize the gastrointestinal tracts of mice attenuates the anticancer effects of PD-1 blockade

<sup>1</sup>Gustave Roussy Cancer Campus, Villejuif Cedex, France. <sup>2</sup>Université Paris-Saclay, Faculté de Médecine, Le Kremlin-Bicêtre, France. <sup>3</sup>Institut National de la Santé Et de la Recherche Médicale (INSERM) U1015, Équipe Labellisée - Ligue Nationale contre le Cancer, Villejuif, France. <sup>4</sup>Department of Gastroenterology and Infectious Diseases, University Hospital Heidelberg, Heidelberg, Germany. <sup>5</sup>Centre de Recherche des Cordeliers, INSERM U1138, Équipe Labellisée - Ligue Nationale contre le Cancer, Université Paris Cité, Sorbonne Université, Paris, France. <sup>6</sup>Metabolomics and Cell Biology Platforms, Gustave Roussy Cancer Campus, Villejuif, France. <sup>7</sup>Centre de Recherche du Centre Hospitalier de l'Université de Montréal (CRCHUM), Montréal, Québec, Canada. <sup>8</sup>Department of Medicine and Surgery, University of Parma, Parma, Italy. <sup>9</sup>Section of Oncology, Department of Medicine, University of Verona School of Medicine and Verona University Hospital Trust, Verona, Italy. <sup>10</sup>Clinical Research Department, Centre Léon Bérard, Lyon, France. <sup>11</sup>EverImmune, Gustave Roussy Cancer Campus, Villejuif Cedex, France. <sup>12</sup>Center of Clinical Investigations in Biotherapies of Cancer (BIOHERIS), Villejuif, France. <sup>13</sup>Clinical Cooperation Unit Applied Tumor Immunity, German Cancer Research Center (DKFZ), Heidelberg, Germany. <sup>14</sup>Department of Medical Oncology, National Center for Tumor Diseases (NCT), Heidelberg University Hospital (UKHD), Heidelberg, Germany. <sup>15</sup>Department of Pediatrics, University Hospital RWTH Aachen, Aachen, Germany. <sup>16</sup>Center of Integrated Protein Science Munich (CIPS-M) and Division of Clinical Pharmacology, Department of Medicine IV, Klinikum der Universität München, LMU Munich, Germany. <sup>17</sup>German Cancer Consortium (DKTK), partner site Munich, Munich, Germany. <sup>18</sup>JBO Consultant, Paris, France. <sup>19</sup>MetaGenoPolis, INRAe, Université Paris-Saclay, Jouy en Josas, France. <sup>20</sup>Institut de Pharmacologie et de Biologie Structurale, IPBS, Université de Toulouse, CNRS, UPS, Toulouse, France. <sup>21</sup>Nantes Université, Université d'Angers, INSERM, CNRS, Immunology and New Concepts in Immunotherapy, INCIT, UMR 1302/EMR6001, Nantes, France. <sup>22</sup>LabEx IGO, Université de Nantes, Nantes, France. <sup>23</sup>Université de Bourgogne Franche-Comté, Plateforme de Transfert de Biologie du Cancer, Centre Georges-François Leclerc, Équipe Labellisée Ligue Nationale Contre le Cancer, Centre de Recherche INSERM LNC-UMR1231, Institut Médical de Génétique et d'Immunologie, Dijon, France. <sup>24</sup>AP-HP, Hôpital Pitié-Salpêtrière, Clinical Investigation Center for Biotherapies (CIC-BTI) and Immunology-Inflammation-Infectiology and Dermatology Department (3iD), Paris, France. <sup>25</sup>Sorbonne Université, INSERM, UMR5959 Immunology-Immunopathology-Immunotherapy Laboratory, Paris, France. <sup>26</sup>Office of Biostatistics and Epidemiology, Gustave Roussy Cancer Campus, Université Paris-Saclay, Villejuif, France. <sup>27</sup>INSERM, Université Paris-Saclay, CESP U1018, Oncostat, labeled Ligue Contre le Cancer, Villejuif, France. <sup>28</sup>Department of Computational, Cellular and Integrative Biology, University of Trento, Trento, Italy. <sup>29</sup>Istituto Europeo di Oncologia (IEO), National Cancer Institute (IRCCS), Milan, Italy. <sup>30</sup>Drug Development Department, Gustave Roussy Cancer Campus, Villejuif Cedex, France. <sup>31</sup>Hematology-Oncology Division, Department of Medicine, Centre Hospitalier de l'Université de Montréal (CHUM), Montréal, Québec, Canada. <sup>32</sup>Institut du Cancer Paris CARPEM, Department of Biology, Hôpital Européen Georges Pompidou, Assistance Publique – Hôpitaux de Paris (AP-HP), Paris, France.

\*Corresponding author. Email: laurence.zitvogel@gustaveroussy.fr (L.Z.); kroemer@orange.fr (G.K.); conrad.rauber@gmx.de (C.Ra.)

†These authors contributed equally to this work.

(7). ACS reduced the expression of most ileal chemokines and *Madcam1* (Fig. 1A and fig. S1A). These effects were specific for the ileum, because they were not observed in the colon or in MCA205 fibrosarcomas (Fig. 1A and fig. S1A). Ileal *Madcam1* mRNA and protein levels were decreased as determined by quantitative reverse transcription polymerase chain reaction (RT-qPCR) (Fig. 1A), immunohistochemistry (Fig. 1B), flow cytometry of ileal CD45<sup>+</sup> LP cells (Fig. 1C and fig. S1B), and enzyme-linked immunosorbent assay (ELISA) of ileal tissue lysates (Fig. 1D). The integrity of the intestinal architecture and vasculature was notably preserved after ACS administration without any alteration in the density of CD31<sup>+</sup> capillaries (fig. S1C). Levels of MAdCAM-1 began to decrease on day 3 of ACS administration and did

not recover on day 4 (ACS+4d) or even on day 12 after ACS cessation (Fig. 1, C and D). The ACS cocktail also down-regulated *Madcam1* gene expression in Peyer's patches and in mesenteric lymph nodes (mLNs) (fig. S1, D and E). Other ABX regimens using  $\beta$ -lactams (ceftazidime and cefepime cephalosporins), aminoglycosides (streptomycin), polymyxins (colistin), and macrolides (erythromycin) also down-regulated ileal *Madcam1* (fig. S1, E and F). By contrast, piperacillin plus tazobactam, rifaximin, and vancomycin had no effect on *Madcam1* expression in two distinct animal facilities located in France (fig. S1E) and Canada (fig. S1F). *Madcam1*, but not vascular cell adhesion protein (*Vcam1*), mRNA levels were 10 times lower in tumor-draining LNs (tdLNs) than in mLNs (fig. S1G). Mass spectrometry of

ileal bacteria cultured from animals treated with various ABX regimens under aerobic and anaerobic conditions identified several species belonging to the genus *Enterocloster* (e.g., *Enterocloster clostridioformis* and *Enterocloster boltea*) (29) that prevailed 4 or 7 days after ACS or erythromycin cessation but not in any other experimental condition (table S1). These *Enterocloster* spp. were previously identified in the stools of cancer patients resistant to PD-1 blockade (10, 11), as well as in chronic inflammatory disorders (30), and mediate resistance to cancer immunotherapy with PD-1 blockade in mice (31). Whereas oral gavage of *E. clostridioformis* reduced ileal *Madcam1* mRNA (Fig. 1E), administration of immunostimulatory *Akkermansia* strain p2261 (*Akk.* p2261) (7, 10) or *Enterococcus hirae* (32) increased

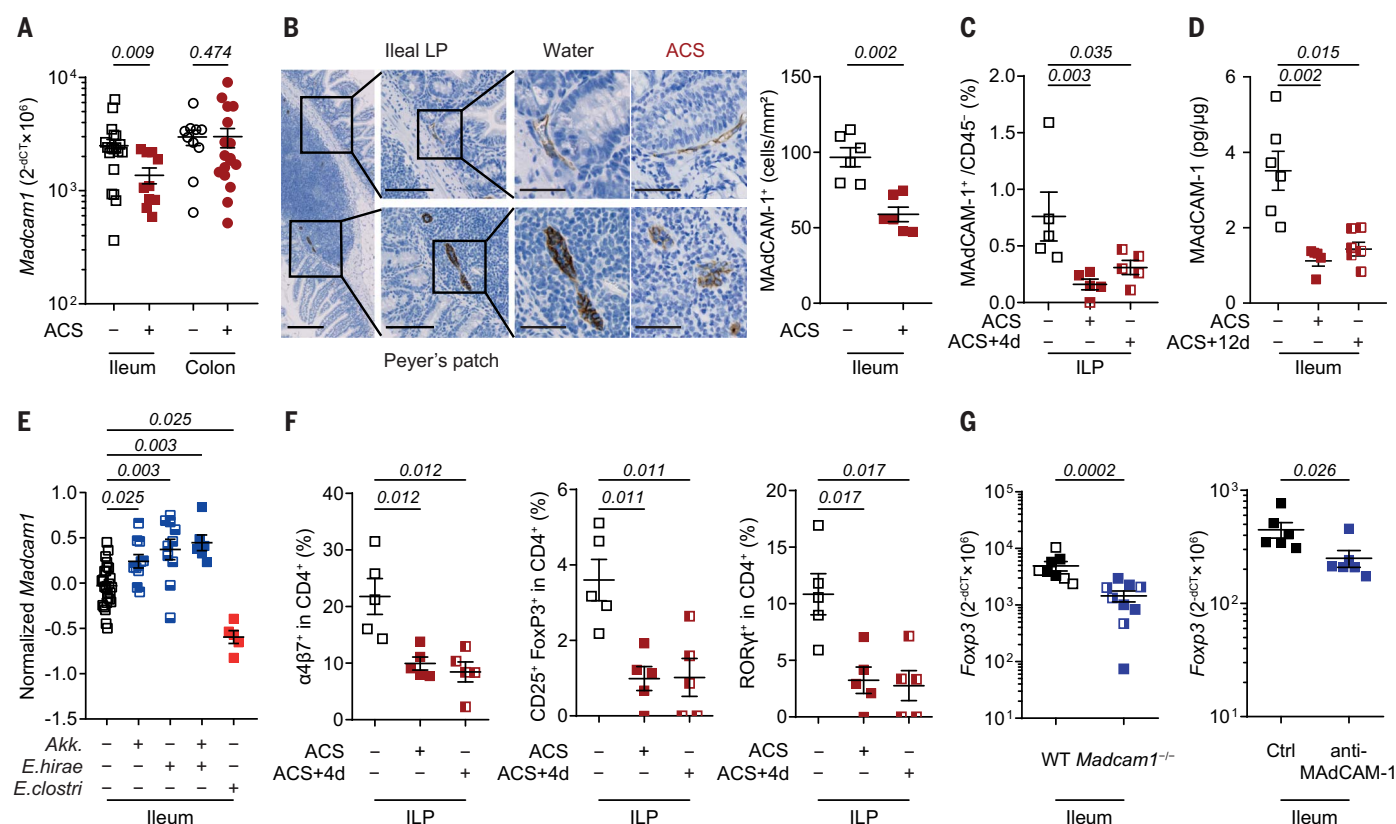


**Fig. 1. Broad-spectrum ABX down-regulate MAdCAM-1 expression in the murine ileal vasculature.** (A to D) Relative transcription (A) and protein (B to D) levels of *Madcam1* gene product obtained with RT-qPCR (A), immunohistochemistry staining of MAdCAM-1 in ileal lamina propria (ILP) venules and high endothelial venules in Peyer's patches in ACS-treated and untreated mice (as indicated above micrograph pictures; scale bars, 200 μm, 100 μm, and 40 μm, respectively) (B), flow cytometry gating on CD45<sup>+</sup> cells of ILP (C), or ELISA (D) of ileal (A to D) or colonic (A) tissues in C57BL/6 mice after continuous ACS, ACS+4d, or ACS+12d spontaneous recolonization, or after cessation of ACS. Each dot represents one ileum [(A) to (D)] or colon (A). *n* = 2 in (A) and *n* = 3 in (B) to (D). (E) RT-qPCR of relative *Madcam1* gene expression normalized on the naive SPF mice group in ileal mucosae of C57BL/6 mice reared in SPF conditions (no ABX conditioning) that underwent oral gavage with bacteria species aligned on the x axis (*n* = 4).

*Akk.*, *Akkermansia* strain p2261; *E. clostri*, *E. clostridioformis*. (F) Same experiments as in (C) performing flow cytometric analysis of ILP CD4<sup>+</sup> T cell subsets (α4β7<sup>+</sup> versus CD25<sup>+</sup> FoxP3<sup>+</sup> T<sub>reg</sub> cells versus RORγt<sup>+</sup> CD4<sup>+</sup> T<sub>H</sub>17 cells) during continuous ACS or at the ACS+4d phase, with each dot representing one ileum. (G) Ileal expression levels of *Foxp3* in *Madcam1* gene-deficient mice (left) or phenocopied with an anti-MAdCAM-1 Ab (right) treated (full dots) or not with anti-PD-1 Ab that did not affect ileal *Madcam1* expression levels (not shown) without ACS conditioning. Each dot represents the RT-qPCR data of one ileum (*n* = 6 mice per group per experiment). (A), (E), and (G) depict a pool of two to three independent experiments. Results from a representative experiment are shown in (B), (C), (D), and (F). Comparisons between groups were analyzed using nonparametric Mann-Whitney *U* test (two groups) or Kruskal-Wallis *H* test (more than two groups) followed by multiple-comparisons test by controlling the FDR. Error bars indicate means ± SEM.



basal *Madcam1* expression in ileal tissues from eubiotic mice reared in specific-pathogen-free (SPF) conditions (Fig. 1E). Moreover, ACS-induced down-regulation of ileal *Madcam1* mRNA correlated with a decrease in regulatory cytokines and transcription factors (e.g., *Foxp3*, *Il17a*, *Il22*, and *Rorc*) (fig. S1, A, H, and I). Consistent with this, ACS depleted mucosal T<sub>reg</sub> and T<sub>H</sub>17 cells from the ileal LP (Fig. 1F and fig. S2A). Finally, ACS phenocopied the ileal immunomodulatory effects of *Madcam1* knockout or antibody neutralization of MAdCAM-1 (Fig. 1G).

We confirmed the coordinated inhibitory effects of several class of ABX on the ileal, but not cecal nor colonic, expression of *MADCAM1*

and *RORC* in 31 patients who were treated with ABX ( $n = 10$ ) compared with nontreated patients ( $n = 21$ ) while they underwent intestinal endoscopy and biopsies for various indications (Fig. 2, A and B, and table S2). As in mice, we found a correlation between *MADCAM1* and *IL17A* ileal mRNA levels (Fig. 2C). In clinical trials, fecal microbial transfer (FMT) from melanoma patients who benefited from PD-1 blockade circumvents primary resistance to ICIs in one-third of metastatic melanoma recipients (33, 34). Moreover, FMT from some human donors fails to improve ICI responses (7, 35). We tested whether random FMT from non-small-cell lung cancer (NSCLC) patients to ABX-preconditioned mice would

modulate ileal *Madcam1* gene expression. Three of six FMTs down-regulated *Madcam1* mRNA (Fig. 2D and table S3). Shotgun metagenomics-based analyses of these three human stools revealed an overrepresentation of *Enterocloster* spp., including *E. clostridioformis*, as well as that of *Hungatella hathewayi*, which is phylogenetically close to *Enterocloster* spp. (29), in two out of three of these stools compared with the three other human fecal samples (Fig. 2D). Mice orally gavaged with stools that down-regulated *Madcam1* expression exhibited a relative over-representation of *E. clostridioformis* (Fig. 2D). Finally, the longitudinal follow-up of cancer patients >60 days after ABX cessation revealed significant decreases of the

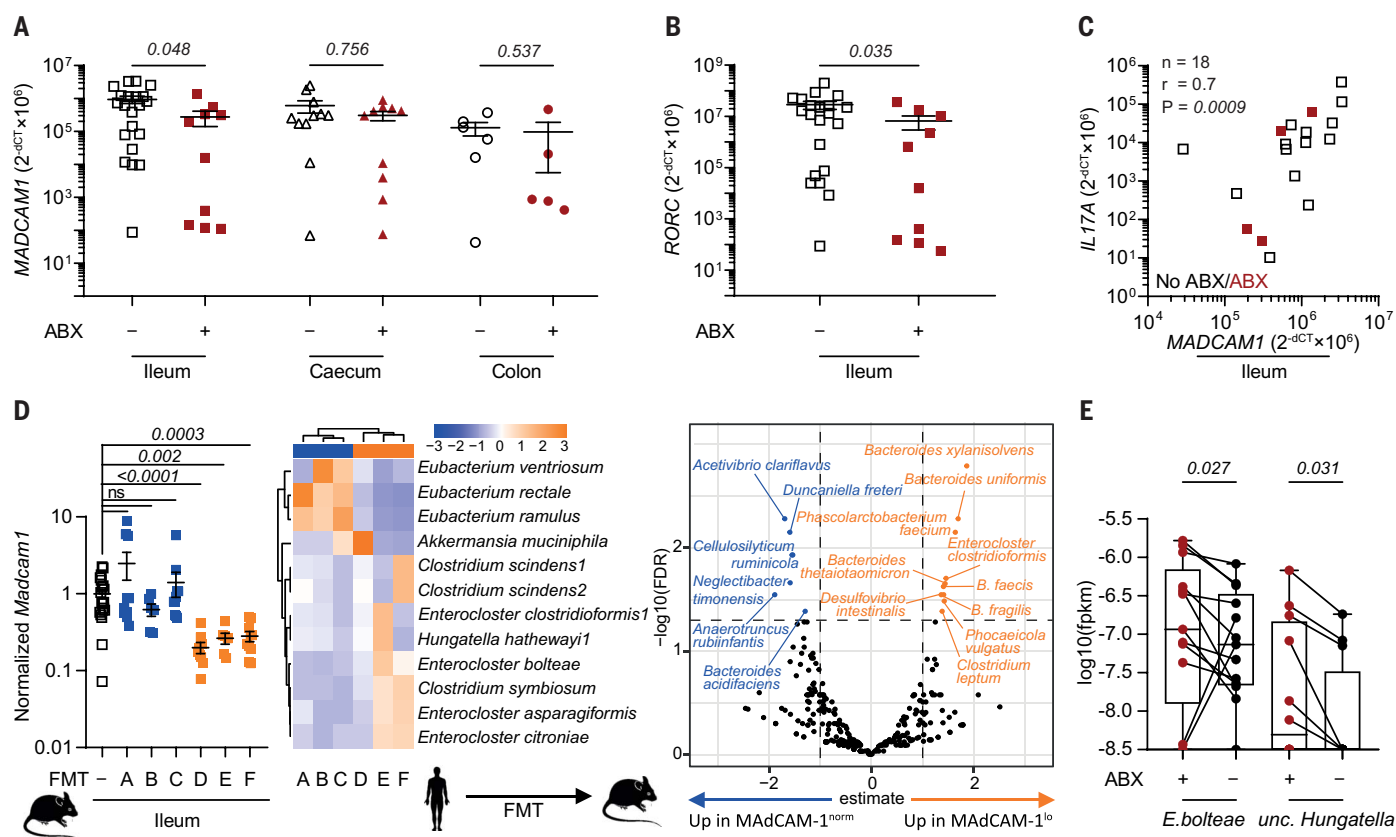


**Fig. 2. Down-regulation of ileal *Madcam1* gene expression in patients taking ABX.** (A and B) RT-qPCR-based transcriptional levels of human *MADCAM1* (A) and *RORC* genes (B) in intestinal biopsies collected during endoscopic intervention in 21 control (ABX-free) patients and 10 ABX-treated patients (table S2). Each dot represents one biopsy from ileum, cecum, or colon, with a single patient being represented one to three times. (C) Spearman's correlation between ileal *IL17A* and *MADCAM1* gene expressions in ABX-treated or untreated patients. (D) Impact of FMT in ABX-treated (3 days) recipient mice using feces from NSCLC patients at diagnosis (before PD-1 blockade) (table S3) on ileal *Madcam1* gene expression normalized on the SPF (FMT-) mice group [log10 axis (D), left panel]. Each experiment used a different FMT donor six times independently and comprised six to 10 animals per group. Each dot represents one ileum. Nonsupervised hierarchical clustering of the taxonomic composition of human donor feces (defined using shotgun MG sequencing), selecting bacteria of high prevalence >25% and clinically relevant (10) [(D), middle panel], and volcano plot contrasting significantly

different stool taxa of FMT-recipient mice, as assessed using 16S rRNA-seq, selecting bacteria of high prevalence and, according to ileal expression levels of *Madcam1* (right panel). Norm, normal levels of MAdCAM-1 (in SPF controls). (E) Shotgun metagenomics-based determination of the relative abundance of fecal species significantly affected by the ABX uptake in lung cancer patients during ABX versus >60 days after ABX discontinuation in a paired analysis including  $n = 13$  individuals. fpkm, fragments per kilo base of transcript per million mapped fragments (gene expression unit). Comparisons between groups were analyzed using nonparametric Mann-Whitney *U* test (two groups) or Kruskal-Wallis *H* test (more than two groups) followed by multiple-comparisons test by controlling the FDR. For (C), nonparametric Spearman's correlation was performed. For the volcano plot in (D), a linear regression was performed to assess *Madcam1* expression as a function of bacteria prevalence in mouse feces and FDR correction was applied. For (E), nonparametric Wilcoxon matched-pairs signed-rank test was performed. Error bars indicate means  $\pm$  SEM.

abundance of *Enterocloster* and *Hungatella* spp. (Fig. 2E). Thus, broad-spectrum ABX down-regulate the expression of the ileal mucosal addressin MAdCAM-1, correlating with reduced ileal *Foxp3*, *Il17a*, and *Rorc*.

To further elucidate potential molecular cues explaining MAdCAM-1 loss after relative dominance of ileal *E. clostridioformis*, we performed mass spectrometric metabolomics of murine ileal contents 7 days after gavage with this bacterium. There were significant changes in biliary acid levels (fig. S3A), consistent with a previous report (36). We screened the effects of various biliary acid (37, 38) and bacteria on *Madcam1* expression in vitro using two murine endothelial cell lines, transformed endothelial sinusoidal cells (TSECs) and brain endothelial cells (bEnd.3), engineered to express green fluorescent protein (GFP) under the control of the *Madcam1* promoter (fig. S3B). Live *E. clostridioformis* directly reduced expression of GFP, whereas the immunogenic *Akk.* failed to do so (fig. S3C). Lithocholic acid (LCA), as well as two synthetic farnesoid X receptor (FXR) agonists, significantly decreased GFP expression in TSEC and bEnd.3 exposed to IL-1 $\beta$  plus tumor necrosis factor- $\alpha$  (TNF- $\alpha$ ) in a dose-dependent manner (fig. S3D). Distinct LCA isoforms reduced GFP expression levels at different dose levels (fig. S3E). RT-qPCR confirmed that LCA down-regulated *Madcam1* mRNA expression levels in TSEC cells (fig. S3F). Moreover, LCA (fig. S3, G and H) and ursodeoxycholic acid (UDCA) (fig. S3I) dampened *Madcam1* gene expression levels in ileum and ileal Peyer's patches and in mLNs in vivo, consistent with a prior report (39). Thus, one of the mechanisms by which *Enterocloster* spp. may down-regulate MAdCAM-1 in GALT is through the accumulation of distinct biliary acids.

#### ABX induce the exodus of enterotropic $\alpha 4\beta 7^+$ CD4 $^+$ T cell subsets to tLNs

We hypothesized that the loss of ileal MAdCAM-1 might affect the trafficking of enterotropic T cells expressing the MAdCAM-1 receptor  $\alpha 4\beta 7$ . We used Kaede mice, which express a fluorescent protein (40) that is photoconverted (PC) upon ultraviolet light (UV) illumination to study the exodus of intestinal cells (20, 22, 23). To track the fate of ileal, cecal, and mLN cells (henceforth referred to as "intestine") 24 hours after photoconversion of tumor bearers, we analyzed PC leukocytes in various organs by flow cytometry (fig. S4A). Up to  $22.8 \pm 2.6\%$  of mLNs cells remained PC $^+$  and PC $^+$  cells became detectable in the spleen ( $5.1 \pm 0.5\%$ ) and tLNs ( $4.0 \pm 0.3\%$ ) (fig. S4A). UV illumination of the ileum also enabled the visualization of gut leukocyte emigration to tLNs or tumors, albeit to a lower extent than intestine illumination (fig. S4B). As a second method of cell tracking, we directly injected carboxyfluores-

cein succinimidyl ester (CFSE) into the mLNs (41) and then followed the emigration of CFSE-labeled cells to distant sites at 24 hours (fig. S4C). Up to  $1.0 \pm 0.2\%$  of splenocytes,  $0.8 \pm 0.1\%$  of tLNs cells, and  $0.2 \pm 0.02\%$  of tumor-infiltrating leukocytes were replaced by mLN-derived leukocytes (fig. S4C). Both methods revealed the selective enrichment of PC $^+$  or CFSE $^+$   $\alpha 4\beta 7^+$  CD4 $^+$  T cells in the spleen, tLNs, and tumor at 24 hours (Fig. 3, A and B, and fig. S4, D and E). Ab-mediated inhibition of MAdCAM-1 in mice led to a more pronounced migration of PC $^+$  or CFSE-labeled cells from the mLNs to the tLNs than in control animals (fig. S4, F and G). By contrast, the migration of mLNs cells to the contralateral LNs (cLNs) was not affected (fig. S4G).

Bulk-RNA sequencing (RNA-seq) of  $\alpha 4\beta 7^{\text{hi}}$  CD4 $^+$  T cells compared with  $\alpha 4\beta 7^-$  CD4 $^+$  T cells purified from mLNs of tumor-bearing mice revealed that  $\alpha 4\beta 7^{\text{hi}}$  CD4 $^+$  T cells overexpressed not only the *Itga4* subunit of  $\alpha 4\beta 7$  but also genes involved in T<sub>reg</sub> cell functions and T<sub>H</sub>17 cell polarization. However, these cells down-regulated *Tnfrsf9* (Fig. 3C and data S1).

We investigated how ACS-induced dysbiosis affected the exodus of CFSE-labeled mLNs cells to tLNs (Fig. 3D). Transient ACS treatment for 14 days, followed by discontinuation of ACS for 4 days, facilitated the mLN to tLN migration of  $\alpha 4\beta 7^+$  T<sub>reg</sub>17 cells, but not that of IL-17A $^+$   $\alpha 4\beta 7^+$  FoxP3 $^-$  CD4 $^+$  conventional T cells or  $\alpha 4\beta 7^-$  T<sub>reg</sub> cells (Fig. 3E, fig. S5A). ACS did not increase the bona fide T<sub>reg</sub> cell pool of the tLNs constituted by the locally expanded (extraintestinal, CFSE $^-$ ) cells (fig. S5B). T<sub>reg</sub>17 cells, which represent up to 40% of intestinal T<sub>reg</sub> cells, constituted the most mobile  $\alpha 4\beta 7^+$  CFSE $^+$  fraction, accounting for  $0.2 \pm 0.1\%$  of all CFSE $^+$  CD4 $^+$  cells reaching the tLNs 24 hours after injection of CFSE into mLNs and after cessation of ACS (fig. S5B). These originally enterotropic T<sub>reg</sub>17 cells not only produced IL-17A but also IL-22 (fig. S5B). *Madcam1* $^{-/-}$  mice also manifested a similar mLN to tLN, but not cLN, migration of CFSE-labeled T<sub>reg</sub> cells (Fig. 3F and fig. S5C). Similarly, in Kaede-transgenic mice subjected to UV illumination of the intestine (fig. S4A), a neutralizing anti-MAdCAM-1 Ab promoted the gut to tLN migration of PC $^+$  CD25 $^{\text{hi}}$   $\alpha 4\beta 7^+$  CD4 $^+$  T cells (Fig. 3G). Because recolonization after ACS is accompanied by the emergence of *Enterocloster* spp. (table S1) that down-regulated ileal *Madcam1* (Fig. 1E), we investigated whether oral gavage with *E. clostridioformis* would be sufficient to trigger this mLN to tLN migration. Indeed, this bacterium facilitated the selective intestinal translocation of PC $^+$ , but not PC $^-$ , CD25 $^{\text{hi}}$  (but not CD25 $^-$ ) T<sub>H</sub>17 cells (CCR6 $^+$ CXCR3 $^-$ ) (Fig. 3H). These findings suggest that the migrating enterotropic T cells do not use MAdCAM-1-expressing high endothelial venules to enter distal tissues. Instead,

we observed a role for L/P-selectins in T cell homing to tumor beds during MAdCAM-1 down-regulation (fig. S6), as previously described (42, 43).

We next performed Rhapsody-based single-cell RNA-seq of CFSE $^+$  CD4 $^+$  T cells recovered from tLNs at 24 hours after CFSE injection into mLNs in mice treated with ACS and oral *E. clostridioformis* (fig. S7, A and B). Unsupervised clustering of the CFSE $^+$  CD4 $^+$  T cells from tLNs partitioned the data into four cellular clusters (fig. S7C and data S2) (44). A small cluster featured the prototypic effector T<sub>reg</sub> cell phenotype (26) (fig. S7D). This T<sub>reg</sub> cell subset overexpressed the genes, *Nrpl*, *Cd39*, and *Cd73*, which are involved in tumor immunosuppression (fig. S7D), and differed from all the other emigrating cells by the overexpression of genes associated with the T<sub>reg</sub>17 cell program (26) (fig. S7D). Another distinctive cluster harbored a follicular T helper/regulatory cell (TFH/TFR)-like transcriptional profile with proliferative/exhaustion hallmarks (45) (fig. S7E). Two other subsets were characterized by a type I interferon (IFN) fingerprint (fig. S7F) and a CD8-like regulatory profile defined by immunosuppressive signaling pathways (46–51) (fig. S7G and data S2).

Most of the mLNs emigrating cells to tLNs were T cells, although some B cells were also observed (Fig. 4A). To address the clonality of T<sub>reg</sub> cells that emigrated from the mLNs, we performed single-cell and deep T cell receptor (TCR) sequencing of CFSE $^+$  T cells harvested from various locations at 24 hours after mLNs CFSE injection. Unsupervised clustering of the CFSE $^+$  T cells partitioned the data into four cellular clusters, one composed of T<sub>reg</sub> cells, one of conventional T cells, and two of CD8 $^+$  T cells (Fig. 4B and fig. S8, A and B). On the basis of the TCR repertoire (52), tumor-infiltrating T<sub>reg</sub> cells, but not conventional T cells, exhibited higher clonal expansion in mice gavaged with *E. clostridioformis* compared with control mice (Fig. 4C). There was a 10-fold increase of TCRs from clusters composed of tumor and tLN TCRs in mice gavaged with *E. clostridioformis* compared with controls, with a concomitant decrease of TCRs from clusters restricted to mLNs (Fig. 4D). This recirculation affected preferentially T<sub>reg</sub> cells over conventional T cells (Fig. 4C). Similar clonal expansions were observed in the CD8 $^+$  population (fig. S8C). The functional profile of mLN T<sub>reg</sub> cells that reached the tumor differed from that of its origin, with an up-regulation of genes involved in immunosuppression, cytolysis, and type I IFN responses (Fig. 4E and fig. S8A). Oral gavage with *E. clostridioformis* significantly increased the proliferative potential of migratory T<sub>reg</sub> cells with the up-regulation of genes implicated in the cell cycle, chromatin silencing, and H3K27 trimethylation, as well as regulatory functions (*Il10*) within tumor beds (Fig. 4, E

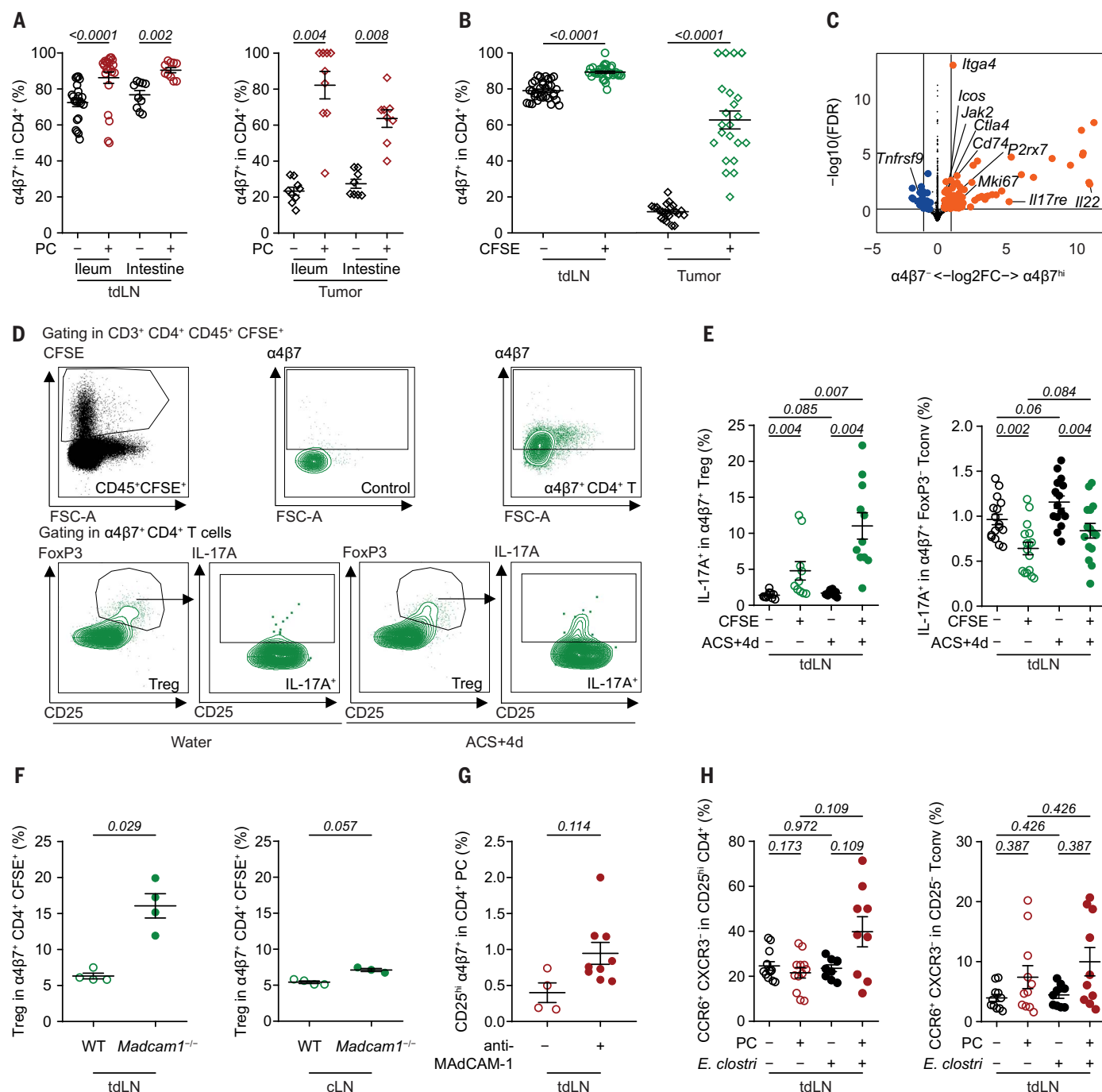


**Fig. 3. ABX-induced exodus of enterotropic  $\alpha 4\beta 7^+$  T<sub>reg</sub>17 cells toward tumor beds.** (A) Flow cytometric analysis of  $\alpha 4\beta 7$  expression in PC<sup>-</sup> or PC<sup>+</sup>  $CD4^+$  T cells residing in the tdLNs or tumor bed in Kaede mice UV illuminated in the ileum or the “intestine” (ileum + cecum + mLNs). (B) Same as in (A) but in WT mice subjected to CFSE injection in the mLNs and gating on CFSE<sup>-</sup> or CFSE<sup>+</sup>  $CD4^+$  T cells. (C) Volcano plot depicting the differential gene transcription in bulk RNA-seq of  $\alpha 4\beta 7^{\text{hi}}$  versus  $\alpha 4\beta 7^{\text{lo}}$   $CD4^+$  lymphocytes cell sorted from mLNs in four MCA205 tumor-bearing animals. Volcano plot was generated computing the log<sub>2</sub> FC ratio of the mean relative abundances of transcripts in  $\alpha 4\beta 7^{\text{hi}}$  versus  $\alpha 4\beta 7^{\text{lo}}$   $CD4^+$  lymphocytes (x axis) with the co-log<sub>10</sub> of *P* values deriving from Mann–Whitney *U* test for each transcript followed by multiple-comparisons test by controlling the FDR. Blue and orange dots are considered significant (*P* < 0.05), whereas back dots are not (*P* > 0.05) (data S1). (D to F) Representative gating strategy and dot plots in flow cytometric

analyses of the IL-17A-secreting  $\alpha 4\beta 7^+$  T<sub>reg</sub> cells (FoxP3<sup>+</sup> CD25<sup>+</sup>),  $\alpha 4\beta 7^+$  conventional T cells (FoxP3<sup>-</sup>),  $CD4^+$  T cells within CFSE<sup>+</sup> (originating from the mLNs, green dots), or CFSE<sup>-</sup> cells (tdLNs resident cells, black dots) reaching the tdLNs during the ACS+4d phase (*n* = 10 to 16 mice per group) [(D) and (E)]. (F) Flow cytometric determination of CFSE<sup>+</sup> T<sub>reg</sub> cells reaching the tdLNs (left) or cLNs (right) in day 7 established MCA205 bearing WT versus *Madcam1*<sup>-/-</sup> mice (not treated with ACS) 24 hours after CFSE injection in mLNs. Each dot represents one mouse. (G) Same as in (F) but in Kaede tumor-bearing mice treated or not with anti-MAdCAM-1 Ab (day 8 after tumor inoculation), photoconverted at day 10. Flow cytometry at day 11 could identify T<sub>reg</sub>-like cells using membrane staining for CD25<sup>hi</sup>. Each dot represents one mouse. (H) Flow cytometric phenotyping of T cells from tdLNs in tumor-bearing mice at day 11 after MCA205 inoculation, gavaged with *E. clostridioformis* (*E. clostri*) at day 8, and photoconverted in the ileum at day 10. The percentages of CXCR6<sup>+</sup>CXCR3<sup>-</sup>



cells in CD4<sup>+</sup> T cells expressing high levels of CD25 (T<sub>reg</sub>17-like, left) or CD25<sup>-</sup> (right) in Kaede mice within PC<sup>+</sup> (originating from the mLNs) or PC<sup>-</sup> cells (tdLN-resident cells) reaching the tdLNs during the colonization phase with *E. clostridioformis*. (A), (B), (E), and (H) show a pool of three to five independent experiments containing five mice per group. Results from a representative experiment are shown in (C), (D), and (F). Each dot

represents one mouse. Comparisons between groups were analyzed using nonparametric Mann–Whitney *U* test (two groups) or Kruskal–Wallis *H* test (more than two groups) followed by multiple-comparisons test by controlling the FDR. For the PC<sup>+</sup> versus PC<sup>-</sup> or CFSE<sup>+</sup> versus CFSE<sup>-</sup> comparisons, Wilcoxon matched-pairs signed-rank test was performed. Error bars indicate mean ± SEM.

and F). The most noticeable commonality between mLNs emigrating CD8<sup>+</sup> and CD4<sup>+</sup> T cells reaching the sarcoma was the shutdown of the translation machinery, as previously reported in exhausted CD8<sup>+</sup> T cells in chronic infection and cancer (53–56) (Fig. 4E, fig. S8, D and E, and data S2). Thus, the enterotropic  $\alpha 4\beta 7^{+}$  CD4<sup>+</sup> T cells that translocate from the mLNs and Peyer's patches to the tdLNs comprise T<sub>reg</sub> and T<sub>reg</sub>17 cells that exhibit immunosuppressive functions. These immunosuppressive programs further increased when the cells reached the tumor bed, in conditions where the MAdCAM-1- $\alpha 4\beta 7$  axis is compromised by neutralization or knockout of MAdCAM-1, recolonization after ABX, or *E. clostridioformis*-induced dysbiosis.

### The anticancer efficacy of PD-1 blockade relies on the MAdCAM-1- $\alpha 4\beta 7$ axis

Given the immunosuppressive role of T<sub>reg</sub>17 cells during cancer immunosurveillance (27, 28, 57), disruption of the MAdCAM-1- $\alpha 4\beta 7$  interaction may interfere with ICI-mediated anticancer effects. Loss of ileal *Madcam1* expression correlated with increased tumor size in tumor-bearing animals regardless of PD-1 blockade (fig. S9A). PD-1 blockade also reduced MCA205 fibrosarcoma growth in wild-type (WT) C57BL/6 mice, but failed to do so in *Madcam1*<sup>-/-</sup> mice and *Itgb7*<sup>-/-</sup> animals, which lack the  $\beta 7$  chain required for the formation of the  $\alpha 4\beta 7$  heterodimer (Fig. 5A). Similarly, MCA205 fibrosarcoma, 4T1 breast, and orthotopic TC-1 lung cancers normally reduced their growth in response to PD-1 blockade but failed to do so after injection of neutralizing anti-MAdCAM-1 or anti- $\alpha 4\beta 7$  Abs (Fig. 5B, C and D). In *Madcam1*<sup>-/-</sup> mice, there was a constitutive increase of  $\alpha 4\beta 7^{+}$  CD4<sup>+</sup> T cells in the spleen and in the tumor, where they represented ~3% of tumor-infiltrating lymphocytes (TILs) (Fig. 5E), as previously described (58). Injection of a neutralizing anti-MAdCAM-1 Ab during spontaneous tumor progression reshaped the TME and led to a threefold increase in the intratumoral accumulation of T<sub>reg</sub>17 cells expressing intestinal T cell markers such as  $\alpha 4\beta 7$ , CCR6, and CCR9 (fig. S9, B and C). Although only 17 ± 0.9% of all MCA205 TILs were  $\alpha 4\beta 7^{+}$ , and 76 ± 1.5% of T<sub>reg</sub>17 cells were  $\alpha 4\beta 7^{+}$  (fig. S9C). In subcutaneous tumors (MCA205, 4T1), T<sub>reg</sub> cells represented 11.7 ± 1.6% of  $\alpha 4\beta 7^{+}$  CD4<sup>+</sup> TILs and, among these T<sub>reg</sub> cells, 44.5 ± 5.3% were ROR $\gamma$ t<sup>+</sup> (table S4). Bacterial recolonization of the gut 4 days after ACS phenocopied *Madcam1* gene

deficiency, inducing a threefold to fivefold increase in the proportion of T<sub>reg</sub>17 cells in tumor beds (Fig. 5, F and G). The tumor-homing behavior of T<sub>reg</sub>17 cells was transient and no longer observed by 12 days after ACS, except when anti-PD-1 Ab was coadministered (Fig. 5H and fig. S9D). Indeed, anti-PD-1 Abs facilitated the priming and/or expansion of T<sub>reg</sub>17 cells in the mLNs in MCA205 tumor-bearing mice (fig. S9E) and contributed to the accumulation of T<sub>reg</sub>17 cells within tumors (Fig. 5H, fig. S9, F and G). In this context, intratumoral T<sub>reg</sub> represented 19.1 ± 2.8% of  $\alpha 4\beta 7^{+}$  CD4<sup>+</sup> TIL and, among these, T<sub>reg</sub> 51.1 ± 7.7% and 61.3 ± 7% were ROR $\gamma$ t<sup>+</sup> and IL-17A<sup>+</sup>, respectively (table S4).

The recruitment of T<sub>reg</sub>17 cells promoted by PD-1 inhibition was further increased when *E. clostridioformis*, but not *Lactobacillus reuteri*, was supplemented by oral gavage after ACS discontinuation (fig. S9H). Blockade of the MAdCAM-1- $\alpha 4\beta 7$  axis during PD-1-targeted immunotherapy impaired the infiltration of tumors by effector CCR5<sup>+</sup> CD8<sup>+</sup> T cells (59, 60) (Fig. 5I). Given that the antimicrobial and pro-inflammatory properties of IL-17, alone or with IL-22 (57, 61), neutralizing these cytokines may circumvent the harmful effects of bacterial recolonization after ABX and during PD-1 inhibition. Indeed, neutralization of IL-17A, but not IL-22RA, counteracted the deleterious effects of ACS on PD-1 blockade (Fig. 5J). Thus, IL-17A plays a role in the immunosuppressive effects of ABX.

### MAdCAM-1 liver expression reduces the tumoral accumulation of enterotropic T<sub>reg</sub> cells

To strengthen the cause–effect relationship between MAdCAM-1 gut expression and emigration of enterotropic suppressive T cells to tumors, we enforced MAdCAM-1 expression in the liver by hydrodynamic injection of *Madcam1*-encoding cDNA inserted into a vector (62). Liver-specific overexpression of the transgene was verified by RT-qPCR and immunohistochemistry (Fig. 6, A and B). Liver expression of MAdCAM-1 correlated with recirculation of the soluble form of MAdCAM-1 (sMAdCAM-1) (fig. S9I). There was a positive correlation between liver *Madcam1* and *Foxp3* mRNA expression or the local presence of FoxP3<sup>+</sup> T cells (Fig. 6C). In ACS-treated mice, enforced hepatic MAdCAM-1 expression reduced the frequency of tumoral  $\alpha 4\beta 7^{+}$ , but not  $\alpha 4\beta 7^{-}$ , T<sub>reg</sub> cells (Fig. 6, D and E). Moreover, high hepatic *Foxp3* expression correlated with a

reduction of tumor size (Fig. 6F). Anti-PD-1 Ab significantly increased liver *Rorc* expression, even more so upon ACS (Fig. 6G), with a positive correlation with liver *Madcam1* (Fig. 6H). Moreover, ACS-induced resistance to anti-PD-1 Abs could be circumvented when mice ectopically expressed *Madcam1* in the liver to locally retain T<sub>reg</sub> cells (Fig. 6I). There was a negative correlation between tumor size and liver *Madcam1* mRNA levels in these conditions (Fig. 6J). Thus, MAdCAM-1 acts as an immune checkpoint controlling the retention of T<sub>reg</sub> cells.

### Soluble MAdCAM-1 is a strong prognostic factor of cancer patient responses

To investigate the clinical relevance of these findings, we first analyzed TIL infiltrates for the presence of enterotropic  $\alpha 4\beta 7^{+}$  T cells in fresh human tumors and ex vivo propagated TILs. The  $\alpha 4\beta 7^{+}$  fraction of T<sub>reg</sub> and CD8<sup>+</sup> T cells represented up to 8.3 ± 2.1% and 24.5 ± 6.9%, respectively, expressed inhibitory receptors and could electively produce IL-17 (fig. S10, A and B). ROR $\gamma$ t<sup>+</sup> FoxP3<sup>hi</sup> cells represented 4.5 ± 0.8% of CD4<sup>+</sup> cells in TILs in expansion and expressed the enterotropic marker  $\alpha 4\beta 7^{+}$  (fig. S10C). On the basis of previous reports (63) and given the correlation between liver or ileal MAdCAM-1 and circulating sMAdCAM-1 levels in mice (fig. S9, I and J), we analyzed the clinical significance of serum sMAdCAM-1 at diagnosis in two independent cohorts of 115 and 187 patients with advanced NSCLC treated with anti-PD-1/PD-L1 antibodies (table S5). Patients treated with ABX exhibited lower sMAdCAM-1 levels than ABX-free patients (Fig. 7A). Baseline serum sMAdCAM-1 was a strong independent prognostic factor of survival in NSCLC patients who did not take ABX and to a lesser extent in those who took ABX before ICIs (Fig. 7B), with high baseline levels associated with prolonged overall survival and progression-free survival (Fig. 7C and fig. S10D). Low sMAdCAM-1 levels identified the subset of PD-1 antibody-refractory patients within PD-L1<sup>hi</sup> (≥50%) NSCLC tumors (Fig. 7D and fig. S10E). Using multivariate Cox regression analysis that took clinical variables into consideration revealed that sMAdCAM-1 is an independent prognostic factor in NSCLC patients (table S5 and table S6). Neither tumor mutational burden nor MER4 retrotransposon elements correlated with sMAdCAM-1 levels (64) (fig. S10F). We validated the clinical significance of serum sMAdCAM-1 as a biomarker of overall survival in 212 metastatic renal cell

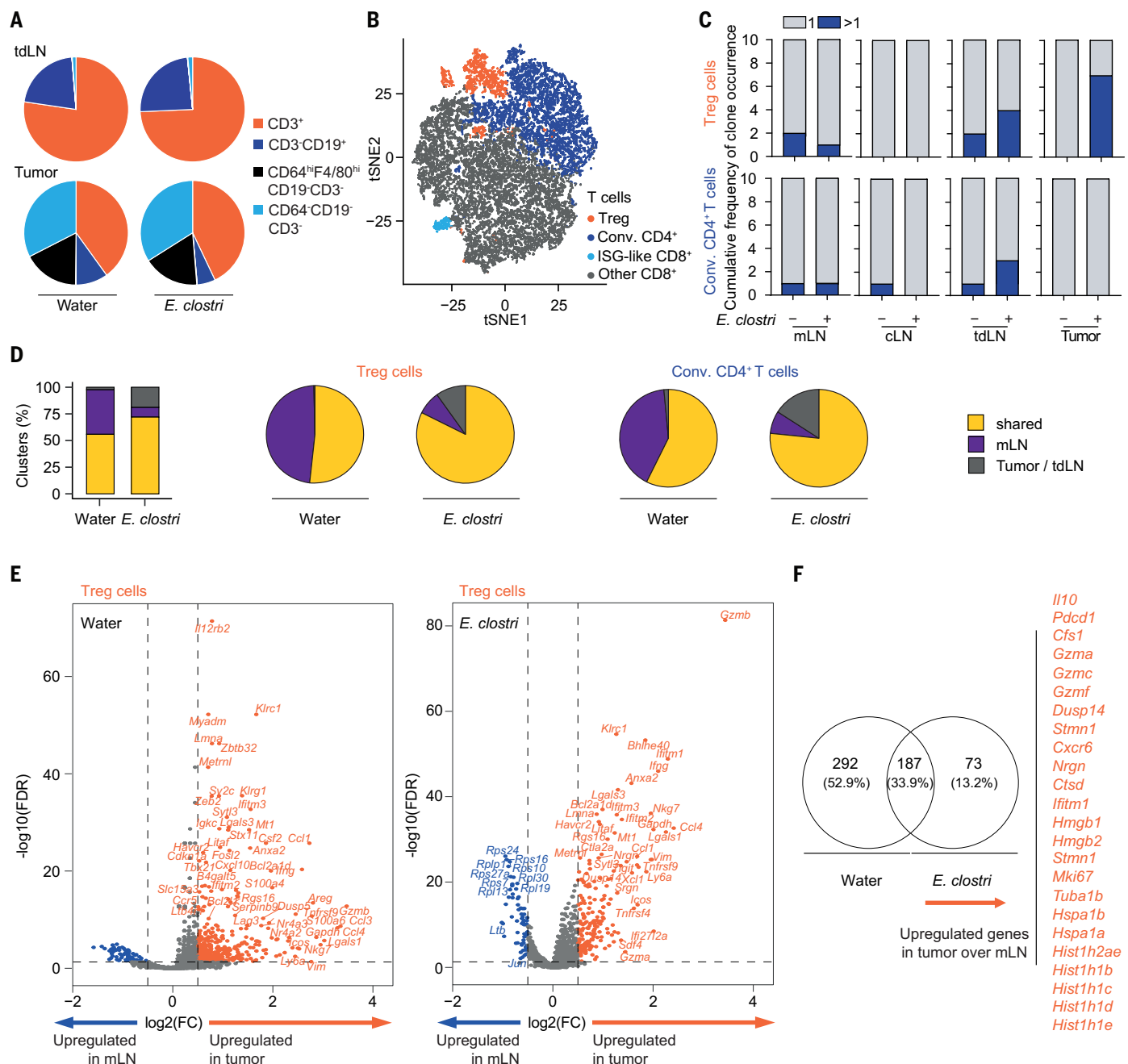


**Fig. 4. Clonal and functional patterns of emigrating T<sub>reg</sub> cells according to locations.** (A) Single-cell sorting and RNA-seq in tumor bearers 11 days after MCA205 implantation using 10X Genomics technology to characterize phenotypic traits of CFSE<sup>+</sup> CD4<sup>+</sup> and CD8<sup>+</sup> T cell subsets emigrating from mLN (CFSE injection at day 10) and reaching tdLN, cLN, or tumor beds, or recovered in mLN after oral gavage with water or *E. clostridioformis* at day 5 and day 7. Determination of CFSE<sup>+</sup> mLN cells emigrating from the gut to the tdLN (top) or tumor beds (bottom) by flow cytometry, according to oral gavage with *E. clostridioformis*, depicted in proportions of all CFSE<sup>+</sup> cells. (B) Single-cell RNA-seq and cell clustering by mean of t-distributed stochastic neighbor embedding (tSNE) of CFSE<sup>+</sup> mLN T cells recovered in mLN, cLN, tdLN, and tumor bed 24 hours after inoculation of CFSE in mLN according to transcriptomic patterns. (C) Single-cell TCR sequencing was performed on CFSE-stained lymphocytes sampled from the mLN, cLN, tdLN, or the tumor. Clones were divided into fractions on the basis of their occurrence in the repertoire. Clones with an occurrence of one are represented in gray, and those with counts higher than one are shown in blue. The cumulative frequency of each fraction was calculated within the repertoire of each

sample. Cumulative frequencies in FoxP3<sup>+</sup>CD127<sup>+</sup> (top) and FoxP3<sup>+</sup> (bottom) CD4<sup>+</sup> T cells according to location are depicted. (D) TCRs from mLN or pooled tumor and tdLN (tumor/tdLN) were clustered with DeepTCR, generating clusters of paired TRA-TRB clonotypes with shared specificities. Clusters were assigned as being mLN (purple), tumor/tdLN (gray), or shared (yellow) on the basis of the percentage of clonotypes composing them. Proportion of mLN, tumor/tdLN, and shared clusters in control (water) and *E. clostridioformis*-gavaged mice (left) and within T<sub>reg</sub> and conventional CD4<sup>+</sup> T cells (middle and right). (E) Volcano plot of differentially expressed genes in CFSE<sup>+</sup> FoxP3<sup>+</sup> CD127<sup>+</sup> CD4<sup>+</sup> T cells in tumors versus mLN (orange versus blue in x axis), in water-treated (left) versus *E. clostridioformis*-treated (right) groups (data S2). (F) Venn diagram comparing control and *E. clostridioformis*-treated groups for genes up-regulated in the tumor (versus mLN), highlighting in orange only those up-regulated in *E. clostridioformis*-treated mice (data S2). Also refer to fig. S8A for detailed CD4<sup>+</sup> T cell phenotypes and subsets and to fig. S8, B, D, and E, for CD8<sup>+</sup> T cell counterparts. (A) depicts a pool of two independent experiments containing six mice per group. Sequencing data [(B) to (F)] were collected once.



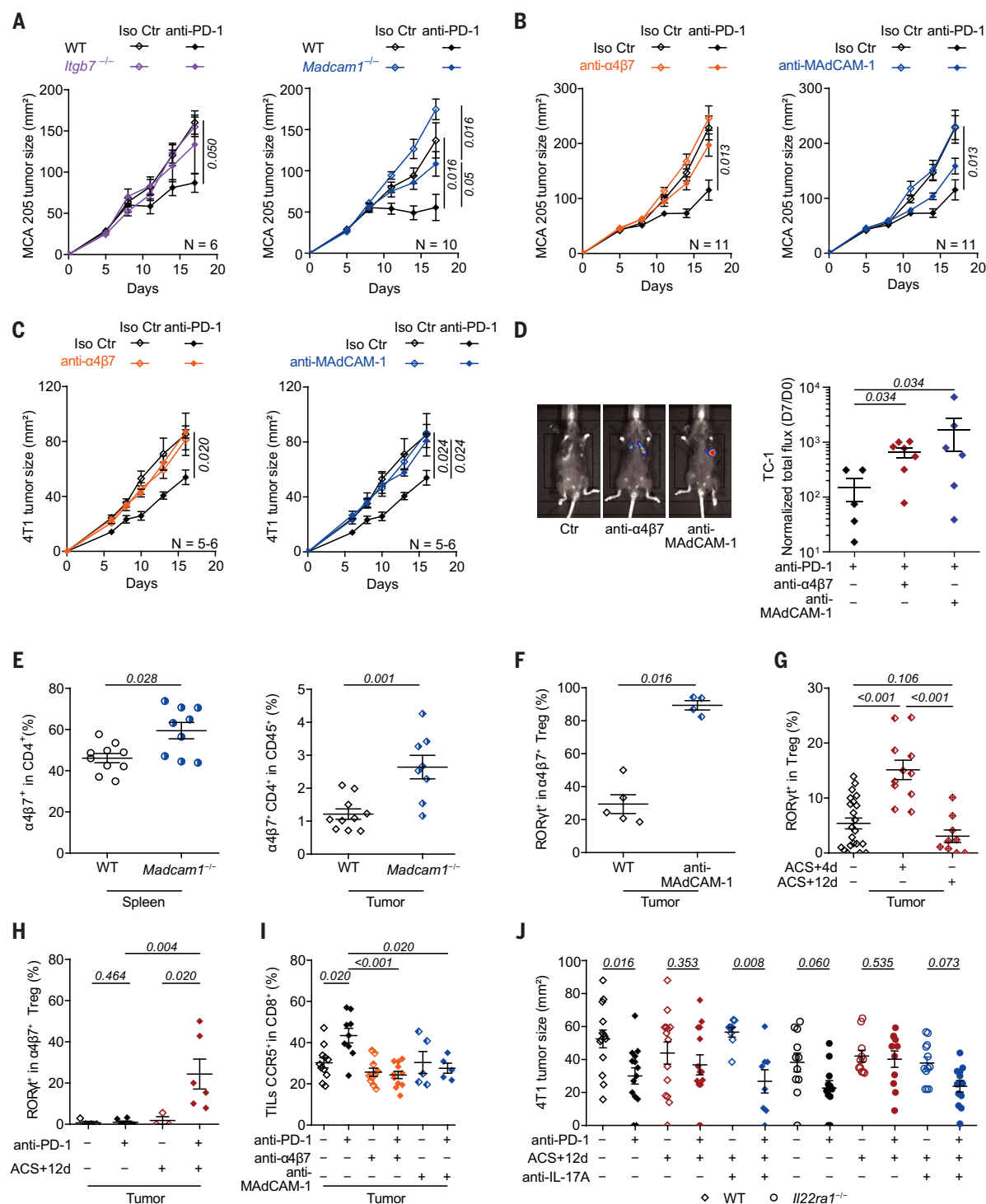


**Fig. 5. Disruption of the MADCAM-1-α4β7 axis induced maladaptive responses to anti-PD-1 Abs in mice.** (A) Tumor growth kinetics of subcutaneous MCA205 (syngeneic of C57BL/6) implanted in WT versus *Itgb7*<sup>-/-</sup> or *Madcam1*<sup>-/-</sup> mice. (B to D) Tumor growth kinetics or whole-body luminescence-based imaging after implantation of subcutaneous (s.c) MCA205 syngeneic of C57BL/6 (B), mammary 4T1 syngeneic of BALB/c (C), and orthotopic luciferase-expressing lung TC-1-luc cancer syngeneic of C57BL/6 (D) in animals treated with isotype control, anti-α4β7 mAb, or anti-MadCAM-1 mAb while receiving anti-PD-1 therapeutic antibodies (or isotype control Abs). For D, ratios between pre- and post-PD-1 blockade with isotype control mAb, anti-α4β7 mAb, or anti-MadCAM-1 mAb were calculated. Shown

are means ± SEM of tumor sizes among five to six mice per group overtime in two treatment groups: anti-PD-1 versus isotype control Ab. (E) Flow cytometric analysis of α4β7 expression on CD4<sup>+</sup> T cell splenocytes and TILs in WT versus *Madcam1*<sup>-/-</sup> mice. Each dot represents one mouse. (F to H) Intracellular flow cytometric analysis of RORγt expression in α4β7<sup>+</sup> or total CD25<sup>+</sup> FoxP3<sup>+</sup> T<sub>reg</sub> TILs in anti-MadCAM-1 or isotype control Ab-treated mice (F) or in WT MCA205 tumor-bearing mice receiving the ACS conditioning regimen (ACS+4d or ACS+12d) treated or not with anti-PD-1 Abs (G and H). (I) Flow cytometric analyses of TILs for CCR5<sup>+</sup> CD8<sup>+</sup> effector T cells in subcutaneous MCA205 tumor-bearing mice treated with isotype control mAb, anti-α4β7 mAb, or anti-MadCAM-1 mAb in the setting of PD-1 blockade.

(J) 4T1 WT or 4T1 *Il22ra1*<sup>-/-</sup> tumor cell lines were inoculated subcutaneously 3 days after starting ACS for 4 days. At ACS discontinuation (after 7 days), neutralizing anti-PD-1 and anti-IL-17A Abs (or isotype control Abs) were injected intraperitoneally five times every 3 days until day 12. Tumor sizes of subcutaneous 4T1 WT or 4T1 *Il22ra1*<sup>-/-</sup> tumors at euthanization. In each experiment, four or five anti-PD-1 intraperitoneal injections were administered every 3 days during the ACS+12d phase. Results from a representative

experiment are depicted in (A) to (D), (F), and (H). Graphs in (E), (I), and (J) contain pooled data of two experiments. Each experiment comprised five to eight mice per group and was performed independently two to four times, leading to similar conclusions. Each dot represents one mouse. Comparisons between groups were analyzed using nonparametric Mann–Whitney *U* test (two groups) or Kruskal–Wallis *H* test (more than two groups), followed by multiple-comparisons test by controlling the FDR. Error bars indicate mean ± SEM.

carcinoma patients under second-line nivolumab (65) (Fig. 7E and table S5) and in 79 patients diagnosed with metastatic bladder cancer treated with durvalumab (anti-PD-L1) (66) (Fig. 7F and table S5).

To demonstrate the relationship between sMAdCAM-1 and gut dysbiosis in advanced NSCLC patients, we performed supervised hierarchical clustering of metagenomics species (MGS) defining the taxonomic composition of the intestinal microbiota using shotgun MG according to the median of sMAdCAM-1 serum levels (199 ng/ml) in 95 NSCLC patients (table S7). MGS richness and Shannon indices were reduced in sMAdCAM-1<sup>lo</sup> (<median) compared with sMAdCAM-1<sup>hi</sup> (greater than or equal to median) patients (Fig. 8A). Moreover, the gut composition diverged between sMAdCAM-1<sup>lo</sup> versus sMAdCAM-1<sup>hi</sup> patients, as indicated by the ANCOM-based beta-diversity (Fig. 8B). Supervised MG analysis revealed two clusters of MGS that were significantly different in relative abundance between the two patient groups (Fig. 8C). Low circulating sMAdCAM-1 levels were associated with an increase in MGS from the genus *Enterocloster* (*E. clostridioformis*), which reduced ileal *Madcam1* expression in mice (Fig. 1E), and *E. bolteae*; both of these species are associated with chronic inflammatory disorders including cancer (30, 31) and poor prognosis in patients treated with immunotherapy (10) (Fig. 8D). Thus, sMAdCAM-1 is a surrogate marker of intestinal dysbiosis and is associated with patient overall survival in advanced bladder, lung, and kidney cancer.

## Discussion

To decipher the mechanisms involved in the immunosuppressive effects of ABX, we studied the emigration of T cells from the gut to distal tumors. We found that the relocation of enterotropic and immunosuppressive T<sub>reg</sub>17 cells to cancer-relevant compartments is at least partially controlled by the molecular interaction between MAdCAM-1 and  $\alpha 4\beta 7$ . This demonstration follows prior evidence that gut-derived T<sub>H</sub>17 cells control extraintestinal autoimmunity (20–24) and inflammation (67, 68). T<sub>reg</sub>17 cells harbor an exacerbated immunosuppressive phenotype compared with conventional T<sub>reg</sub> cells (26). Recent intestinal T<sub>reg</sub>17 emigrants found in tDLNs exhibit gut-specific T<sub>reg</sub> cell features (69, 70), T<sub>H</sub>17 cell-related gene expression patterns (71), as well as immunosuppressive traits such as *Dusp2*/

PCAI (47) and *Pik3ip1* (72). In tumors or tDLNs, gut T cell emigrants shut down protein translation and acquire features of exhaustion or lytic functions, perhaps reflecting chronic TCR stimulation (56). These data collected in tumor-bearing hosts may be interpreted in the context of inflammatory bowel disease, in which the anti- $\alpha 4\beta 7$  Ab vedolizumab increases the recirculation of extraintestinal  $\alpha 4\beta 7^{+}$  T<sub>reg</sub> cells and central memory T<sub>H</sub>17 cells (73–75). However, on the basis of our results,  $\alpha 4\beta 7$  neutralization may have undesirable systemic immunosuppressive effects in the context of intestinal dysbiosis. Thus, prospective studies should monitor circulating sMAdCAM-1 and  $\alpha 4\beta 7^{+}$  T<sub>reg</sub>, T<sub>reg</sub>17, and T<sub>H</sub>17 cells in cancer patients treated with ICIs alone or in combination with FMT or vedolizumab to correlate these parameters with efficacy and toxicity.

## Materials and Methods

### Patient characteristics and clinical description

#### Medical centers and regulatory approvals for translational research

For feces and serum collection, ancillary studies were conducted at Gustave Roussy Cancer Campus (GRCC), France according to the ethical guidelines and approval of the local Committees for the Protection of Persons in Biomedical Research (CCPRB). The ONCOBIOTICS trial (www.clinicaltrials.gov, NCT04567446, ID-RCB no. 2017-A02010-53), a multicentric prospective observational study, was designed to evaluate the impact of the microbiome composition in the clinical outcome of patients with advanced NSCLC treated with anti-PD-(L)1 (10). We enrolled patients across 12 academic centers in France and two centers in Canada. Adult patients with pathologically confirmed advanced nonsquamous or squamous NSCLC and an Eastern Cooperative Oncology Group (ECOG) performance status score of 0 to 2 amenable to ICI as standard of care and willing to provide a stool sample were eligible. Eligible patients received ICI after progression on platinum-based chemotherapy regimens either with nivolumab or atezolizumab regardless of PD-L1 expression or with pembrolizumab if PD-L1 ≥ 1%. Given the subsequent approval of first-line ICI during the study accrual period, patients who received pembrolizumab monotherapy or in combination with platinum-based chemotherapy, depending on PD-L1 expression, were also included. Standard of care treatment was continued until disease

progression, unacceptable adverse effects, or completion as per protocol (2 years of ICI). Full eligibility criteria are listed in the trial protocol (available at www.clinicaltrials.gov, NCT04567446). Baseline characteristics, including a detailed listing of concurrent medications received over the past 2 months before ICI initiation and the date of last follow-up, were entered at each center in an electronic case report form. Feces were collected according to the International Human Microbiome Standards (IHMS) guidelines (SOP 03 V1) before the first injection. Serum samples were prospectively collected after prior anti-PD(L)1 immunotherapy within the Gustave Roussy Cancer Campus-sponsored PREMIS study (www.clinicaltrials.gov, NCT03984318). Patients enrolled in PREMIS were ≥18 years of age, with histologically proven solid malignancy and at least one tumor evaluation by imaging after immunotherapy onset. The PREMIS study was approved by an ethical committee (Comité de Protection des Personnes Sud-Ouest et Outre Mer I; ID-RCB: 2018-A01257-48) and the institutional review board (CSET no. 2018/2728). All enrolled patients provided a signed informed consent. Furthermore, we disposed of one cohort of 45 patients with NSCLC receiving treatment with anti-PD-1/PD-L1 checkpoint inhibitors between 2014 and 2020. Patients were treated in the Georges François Leclerc Cancer Center. For all patients, abundance of transcripts from RNA-seq data was available, and for some patients, PD-L1 protein expression in tumor cells assessed using immunohistochemistry was also available, as well as tumor mutational burden estimated from whole-exome sequencing. We had access to a cohort of patients with advanced renal cell carcinoma treated with an anti-PD-1 enrolled in the NIVOREN trial (www.clinicaltrials.gov, NCT03013335; EudraCT: 2015-004117-24). Finally, an additional cohort of patients with bladder cancer treated with an anti-PD-(L)1 alone or together with anti-CTLA-4 and enrolled in the IOPREDI study (EudraCT 2016-005068-33) was studied. For tumor flow cytometric analyses of fresh or cultivated TILs, all tumor tissues were processed according to the Helsinki Declaration and the guidelines of the French ethics Committee for Research on Human Tissues. Tissue biocollection was registered with the French Ministry for Higher Education and Research (DC-2014-2206) with approval from the ethics committee (CPP Ouest IV, Nantes).

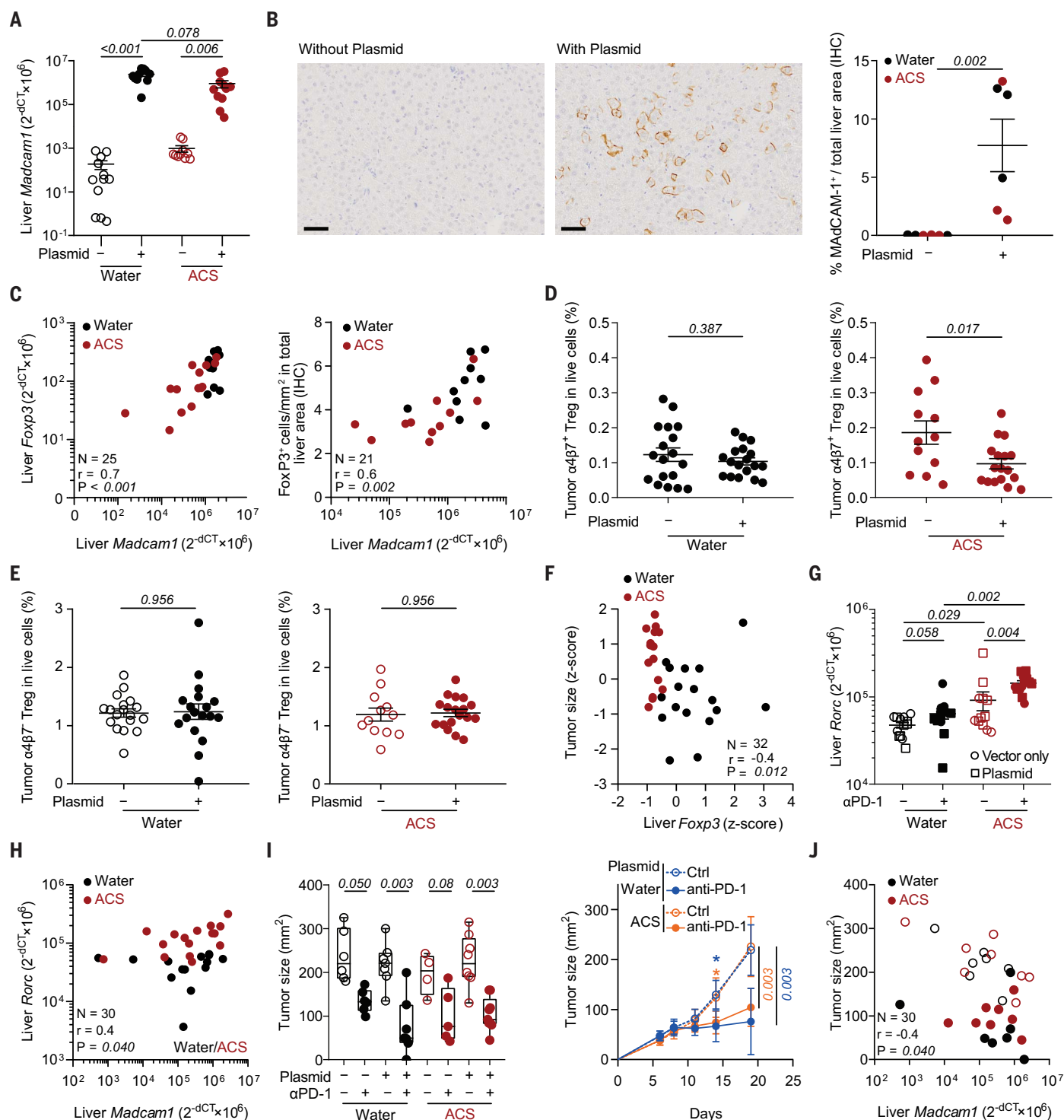


**Fig. 6. Interception of immunosuppressive T cells by transfection-enforced overexpression of MadCAM-1 in the liver.** The experiment involved rapid hydrodynamic intravenous injection of *Madcam1*-encoding cDNA subcloned into a pLIVE plasmid vector (plasmid+) or vector alone (plasmid-) into day 5 tumor-bearing mice preconditioned with ACS for 3 to 4 days (or with water from day -3 to day +5) and treated [(G) to (J)] or not [(A) to (F)] with four intraperitoneal inoculations of anti-PD-1 Ab from day 6 to day 14. **(A and B)** Liver expression of *Madcam1* mRNA (A) or MADCAM-1 protein (B) as assessed by RT-qPCR (A) or immunohistochemistry (IHC) (B) according to plasmid inoculation and ACS treatment. One representative micrograph is shown for

immunohistochemistry [(B), left]. Scale bar, 40  $\mu\text{m}$ . **(C)** Spearman's correlations between liver *Foxp3*/FoxP3 in RT-qPCR (left), immunohistochemistry (right), and *Madcam1* mRNA (RT-qPCR) relative expression in plasmid-treated mice. **(D and E)** Flow cytometric analysis of  $\alpha 4\beta 7^+$  (D) or  $\alpha 4\beta 7^-$  (E)  $T_{\text{reg}}$  cells in water or ACS-treated mice according to *Madcam1*-encoding cDNA plasmid injection (or control vector). Shown are concatenated mean  $\pm$  SEM percentages of stained T cells. **(F)** Spearman's correlation between liver *Foxp3* in RT-qPCR after normalization of relative expression (z score), and tumor size at euthanization (day 14). **(G and H)** Liver expression of *Rorc* and *Madcam1* relative gene expression in RT-qPCR according to PD-1 blockade and *Madcam1*-encoding cDNA



plasmid injection (or control vector) as well as ACS (or water). (H) Spearman's correlation between liver *Rorc* and *Madcam1* relative gene expression in RT-qPCR in plasmid-treated mice. (I and J) Tumor size in MCA205-bearing animals treated with anti-PD-1 Abs in water or ACS-treated mice according to *Madcam1*-encoding cDNA plasmid injection (or control vector) [(I), left]. Tumor growth kinetics in MCA205-bearing animals treated with anti-PD-1 Abs with or without ACS in animals inoculated with the vector alone or the *Madcam1*-encoding cDNA plasmid [(I), right]. (J) Spearman's correlation between liver *Madcam1* relative expression in RT-qPCR and tumor size at

euthanization (day 19) in plasmid-treated mice. Except for (B), which shows a representative experiment, graphs depict the data pooled from two independent experiments containing six to 10 mice per group. Each dot represents one mouse. Black and red dots represent water- and ACS-treated animals, respectively. Comparisons between groups were analyzed using nonparametric Mann-Whitney *U* test (two groups) or Kruskal-Wallis *H* test (more than two groups) followed by multiple-comparisons test for controlling the FDR and nonparametric Spearman's correlations. Error bars indicate means  $\pm$  SEM.

Each patient included in this study signed an informed consent form. For the four fresh NSCLC tumors examined by flow cytometry,  $\geq 18$ -year-old patients from Gustave Roussy Cancer Campus, Marie Lannelongue, Cochin, Tenon, Foch, Kremlin-Bicêtre, and Saint Joseph hospitals with primary resectable tumors provided written informed consent according to the protocols reviewed and approved by institutional ethics committee, including the investigator-sponsored, study "mAb in vitro test" (ID-RCB: 2016-A00732-49). The experiments conformed to the principles set out in the Declaration of Helsinki and the Department of Health and Human Services Belmont Report. For collection of endoscopic and blood samples, a clinical study, "Einfluss von Antibiotika auf das Darm-Chemokinnetzwerk bei Patienten mit soliden Tumoren," was conducted at University Clinics Heidelberg, Germany, according to the ethical guidelines and approval of the Regierungspräsidium Karlsruhe.

#### Collection of endoscopic samples and blood samples

Eligible patients underwent ileocolonoscopy according to clinical standard protocols for non-study-related indications (table S2) between July 2018 and November 2019. When feasible, endoscopic biopsies of the mucous membranes of the terminal ileum, cecum, and right and left colons were performed in each patient. Tissue samples were either snap frozen in liquid nitrogen and stored at  $-80^{\circ}\text{C}$  or immersed into 2% paraformaldehyde (PFA) for histology. In addition, two blood samples (10 ml in EDTA tubes) were collected before ileocolonoscopy. All included patients responded to a questionnaire to assess dietary history, and baseline clinical data were retrieved from the local clinical information system.

#### Metagenomic analysis of patient stools

Fecal samples were prospectively collected at different time points (V1, before ICI; V2, before the second ICI injection; V3, 3 months after ICI; and V4, 6 months after ICI) at each center following the International Human Microbiome Standards (IHMS) guidelines, but only the baseline V1 sample was considered for this analysis. For metagenomic analysis, the stools were processed for total DNA extraction and sequencing with Ion Torrent technology follow-

ing MetaGenoPolis (INRAE) France, as previously reported (7, 10, 11). The gene abundance table was processed using the MetaOMineR (momr R) package. We conducted PERMANOVA using the function *adonis* from the *vegan* R package (v2.5-7) with the Atchinson distance on centered log ratios using species-level abundances and 1000 permutations. We used an ensemble of univariate and multivariate differential abundance methods that included age, gender, and cohort in the models, using either species-level relative abundances or count data, where absolute raw counts were estimated from species-level relative abundances by multiplying these values by the total number of reads for each sample. These differential abundance methods included; DESeq2 (v1.30.0) (76) with the poscounts estimator (DESeq2\_poscounts); DESeq2 with the poscounts estimator and a zero-inflated negative binomial model (DESeq2\_poscounts\_zb); DESeq2 with trimmed mean of M values (TMM; DESeq2\_TMM); limma (v3.46.0) (77) with TMM values (limma\_voom\_TMM); limma with TMM values and a zero-inflated negative binomial model (limma\_voom\_TMM\_zb); ANCOM-BC (v1.0.1) (78); and Maaslin2 (v1.4.0) (79) and LeFSE (80).

#### sMAdCAM-1 quantification in patients

sMAdCAM-1 was quantified in patient sera with the Bio-Plex 200 systems (Bio-Rad) and sMAdCAM-1 kit from R&D Systems (Human Luminex Discovery Assay LXSAM).

#### Cell culture, reagents, and tumor cell lines

MCA205 fibrosarcoma cells (syngeneic from C57BL/6 mice) and 4T1 WT and 4T1-*Il22ra1*<sup>-/-</sup> breast cancer cell lines [syngeneic from BALB/c, kindly provided by Dr. S. Kobold (57), LMU Klinikum, Germany] were cultured at  $37^{\circ}\text{C}$  in the presence of 5%  $\text{CO}_2$  in RPMI 1640 containing 10% fetal calf serum (FCS), 2 mM L-glutamine, 100 IU/ml penicillin-streptomycin, 1 mM sodium pyruvate, and minimum essential medium nonessential amino acids (henceforth referred to as complete RPMI 1640). Luciferase-transfected TC-1 cell lines syngeneic for C57BL/6 mice [kindly provided by E. Deutsch, GRCC] were cultured at  $37^{\circ}\text{C}$  in the presence of 5%  $\text{CO}_2$  in complete RPMI 1640 and 1 mM Hepes buffer. Cell lines were regularly tested for mycoplasma contamination and were not used after 10 passages.

#### Mice

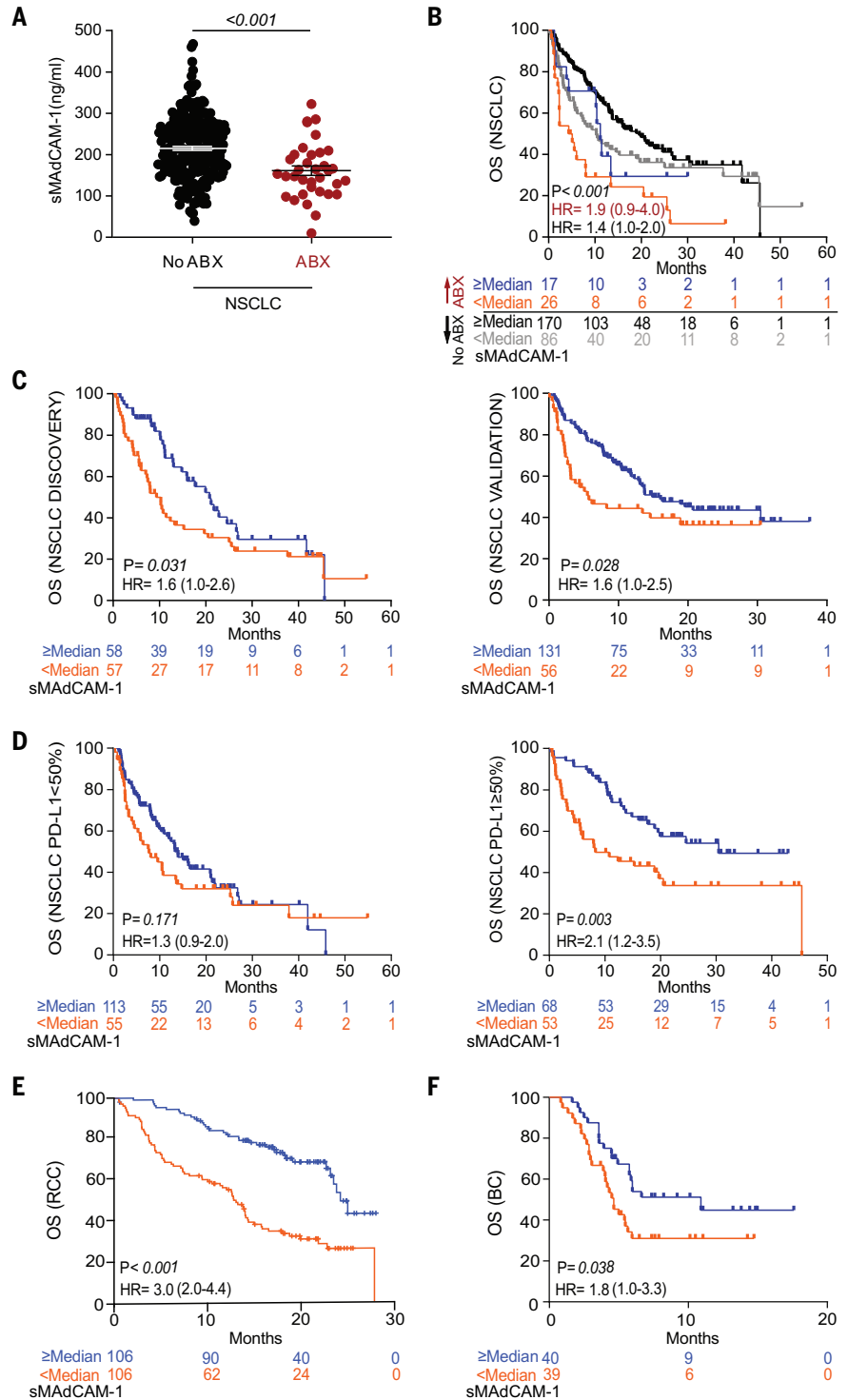
All animal experiments were performed in compliance with French and European laws and regulations. The local institutional animal ethics board and French Ministère de la Recherche approved all mouse experiments (permission numbers: 2016-049-4646, 2017\_049\_99741, 2019\_036\_21124, and 2022\_064\_40164). Experiments were performed in accordance with Government and institutional guidelines and regulations. Female C57BL/6 and BALB/c mice were purchased from Harlan or Envigo (France). Mice were used between 7 and 12 weeks of age. *Madcam1*<sup>-/-</sup> and *Itgb7*<sup>-/-</sup> mice were a kind gift from A. Schippers (University Hospital Aachen, Aachen, Germany). *Madcam1*<sup>-/-</sup> and *Itgb7*<sup>-/-</sup> mice and control littermates were backcrossed on the C57BL/6 background and were obtained from an in-house breeding at the local animal care facility at the University Hospital Aachen. The Kaede mice were a kind gift from M. Tomura (Kyoto University, Kyoto, Japan) and were backcrossed and maintained on the C57BL/6 background. All mouse experiments were performed at the animal facility at the GRCC, where animals were housed in SPF conditions.

#### Antibiotic treatments

If not otherwise indicated, mice were treated with a broad-spectrum ABX solution containing ampicillin (1 mg/ml), streptomycin (5 mg/ml), and colistin (1 mg/ml) (Sigma-Aldrich) (ACS) added to sterile drinking water. In experiments in which single antibiotics were used, the concentrations were identical as stipulated above for ampicillin (A), colistin (C), or streptomycin (S), and were 1 mg/ml for erythromycin, 0.25 mg/ml for vancomycin, 6.15 mg/ml for ceftazidime, 4.1 mg/ml for cefepime, 16.4/2.05 mg/ml for piperacillin/tazobactam, and 1.13 mg/ml for rifaximin. Solutions and bottles were changed three times weekly. In the experiments in which the antibiotic mixture was used, antibiotic activity was confirmed by cultivating fecal pellets for 48 hours at  $37^{\circ}\text{C}$  in aerobic and anaerobic conditions. To evaluate the impact of antibiotics on MAdCAM-1 expression in the intestine, ACS were administered during 7 to 14 days and discontinued for 4 days (ACS+4d) or for 12 days (ACS+12d) or were continued until the end of the experiment in the drinking water of naive or MCA205 tumor-bearing mice.

**Fig. 7. Serum-soluble MAdCAM-1 is a robust prognosis parameter in cancer patients.**

(A) Luminex immunoassay monitoring of serum levels of sMAdCAM-1 in 299 NSCLC patients belonging to two independent cohorts according to history of recent ABX uptake (tables S5 and S7). Each dot represents one patient's serum. Error bars represent means  $\pm$  SEM. (B to D) Overall survival (OS) analysis using the Kaplan Meier estimator and Cox regression to assess the prognostic value of serum levels of sMAdCAM-1, split using the median of the NSCLC patient discovery cohort amenable to PD-1 blockade, according to ABX uptake history (B). This cut-off determined from the discovery cohort allowed us to split the patients into two groups of different prognosis in the validation cohort (C). (D) Idem as in (C) combining both cohorts of NSCLC and segregating patients according to tumor PD-L1 expression and the cut-off value of sMAdCAM-1 (median of the discovery cohort) (see table S5 for patient descriptions, table S6 for multivariable analysis, and fig. S10, D and E, for progression-free survival). (E) Same as in (C) but overall survival in 212 in second- or third-line metastatic renal cell carcinoma (RCC) patients amenable to nivolumab. (F) Same as in (C) but overall survival in 79 patients diagnosed with metastatic bladder cancer (BC) treated with durvalumab (anti-PD-L1). Kaplan-Meier overall survival curves were generated, and hazard ratios (HRs) are indicated.



**FMT experiments**

In FMT experiments, mice received 3 to 7 days of ACS before undergoing FMT the next day by oral gavage. FMT was performed by thawing fecal material. Mice were placed in a new cage after the procedure. Two hundred microliters of the suspension was then transferred by oral gavage into each ACS-pretreated recipient using

animal-feeding needles. In addition, another 100  $\mu$ l was applied to the fur of each animal.

**Oral bacterial gavage with commensal species**

*Akk.* p2261 was provided by everImmune (Villejuif, France). *E. hirae* 13144 isolates were originally isolated from spleens or mLN of SPF mice treated with cyclophosphamide at GRCC.

*E. clostridioformis* was isolated from the ileum of mice that received ACS in drinking water for 7 days followed by 4 days ABX-free at GRCC. *Akk.* p2261, *E. clostridioformis*, and *L. reuteri* were grown on Columbia agar with 5% sheep blood (COS) plates in an anaerobic atmosphere created using three anaerobic generators (Biomérieux) at 37°C for at least 72 hours. *E. hirae*

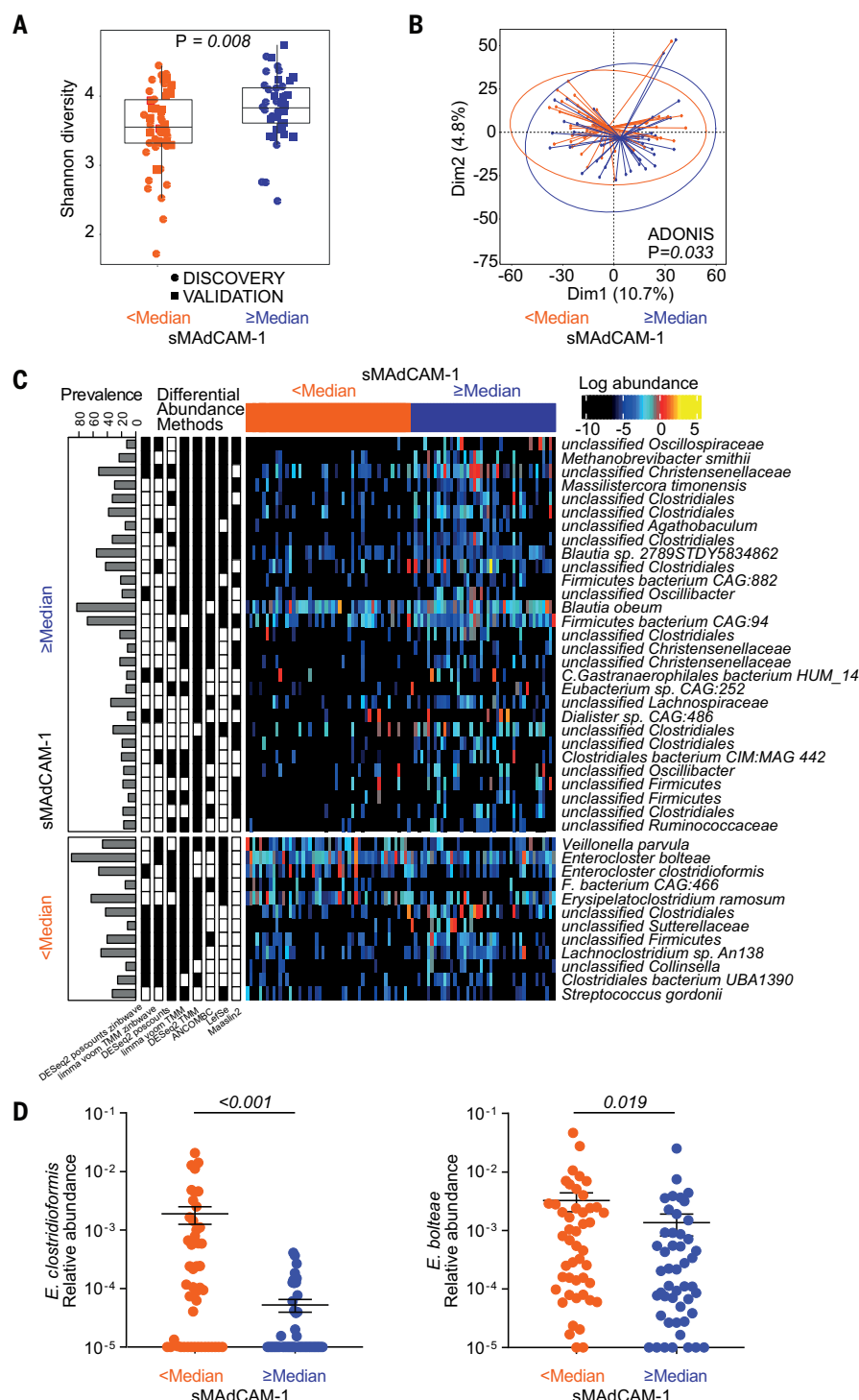


**Fig. 8. Serum sMAdCAM-1 is a proxy for gut dysbiosis.** (A and B) Alpha (A) and beta (B) diversity of the taxonomic content of the intestinal microbiota according to the serum sMAdCAM-1 levels in 95 NSCLC patients. (A) MGS Shannon diversity evaluation in shotgun MG sequencing according to the median of sMAdCAM-1 in the whole population composed of 95 NSCLC patients (refer to table S7 for patient description). The *P* value was calculated by a Wilcoxon test blocking for cohort. (B) Principal-component analysis of species-level centered log-ratio-transformed relative abundance. The *P* value was calculated using ADONIS and 999 permutations. (C) Differentially abundant species according to sMAdCAM-1 serum levels (< low; ≥ high according to median) color coded according to the relative abundance of each species detected by at least three different methods. (D) Relative abundances of two distinct species from the genus *Enterocloster*, categorizing the patients according to the median of sMAdCAM-1. Each dot represents each patient's stool. Comparisons between groups were analyzed using the nonparametric Mann-Whitney *U* test (two groups). Error bars indicate means ± SEM.

13144 was grown in 5% sheep blood enriched Columbia agar for 24 hours at 37°C in aerobic conditions. Colonization of SPF C57BL/6 mice was performed by oral gavage with 100 µl of suspension containing  $1 \times 10^8$  to  $1 \times 10^9$  bacteria. Bacteria concentrations were calculated using a fluorescence spectrophotometer (Eppendorf) at an optical density of 600 nm in 0.9% NaCl. Mice were gavaged one to four times. In applicable experiments, oral gavages were performed concomitantly with anti-PD-1 Ab treatment four times. The identification of specific bacteria was accomplished using a matrix-assisted laser desorption/ionization-time-of-flight (MALDI-TOF) mass spectrometry (Bruker, France).

#### Oral gavage with biliary acids

Mice were gavaged four times every 2 days with 120 mg/kg body weight LCA (ThermoFisher Scientific, 229090050) or UDCA (Delursan, Teva Santé) diluted in corn oil.

#### Subcutaneous cancer mouse models

##### MCA205 sarcoma and 4T1 WT and *Il22ra1*<sup>-/-</sup> breast cancer

Syngeneic C57BL/6 mice were implanted with  $0.8 \times 10^6$  MCA205 sarcoma cells subcutaneously and treated intraperitoneally when tumors reached 20 to 40 mm<sup>2</sup> in size with anti-PD-1 mAb (250 µg/mouse; clone RMP1-14) or isotype control (clone 2A3). Syngeneic BALB/c mice were implanted with  $0.5 \times 10^5$  4T1 WT or *Il22ra1*<sup>-/-</sup> breast cancer cells subcutaneously and treated intraperitoneally with anti-PD-1 or isotype control mAbs. Mice were injected four times at 3-day intervals with anti-PD-1 (Bio X Cell, clone RMP1-14, 250 µg per mouse) or isotype control (Bio X Cell, clone 2A3, 250 µg per mouse) mAbs. Tumor length and width were routinely monitored three times a week by means of a caliper. In experiments using anti-α4β7 mAb (DATK32, 200 µg per mouse), anti-MAdCAM-1 mAb (MECA-367, 200 µg per mouse), or their isotype controls (clone 2A3 in both cases), monoclonal Abs were injected intraperitoneally every 3 days starting from day 0 until the final anti-PD-1 injection. In the experiment using anti-IL-17A mAb (clone IL-17F, 100 µg per mouse), mice were injected intraperitoneally concomitantly with anti-PD-1 treatment. All antibodies were purchased from Bio X Cell. In the experiment using anti-CD62L or anti-PSGL-1 mAbs (clones Mel-14 and 4RA10, respectively, 100 µg per mouse), mice were injected intraperitoneally concomitantly with anti-MAdCAM-1 treatment.

#### Orthotopic luciferase engineered-TC-1

C57BL/6 mice were anesthetized with isoflurane. Under sterile conditions, a lateral incision was made on the chest wall of each mouse, and  $6 \times 10^5$  TC-1-Luc cells in 10 µl of Matrigel



(Corning) were injected into the lung. The skin incision was closed with a surgical skin clip. To monitor tumor growth twice weekly, mice received a percutaneous injection of luciferase substrate (beetle luciferin, potassium salt; Promega) at a dose of 150 mg/kg body weight. Eight minutes after luciferin inoculation, photons were acquired on a Xenogen IVIS 50 bioluminescence in vivo imaging system (Caliper Life Sciences Inc., Hopkinton, MA, USA).

#### *Construction of liver-specific overexpression vector*

The plasmid pLIVE vector was purchased from Mirus (catalog no. MIR 5420, Madison, WI, USA), and Madcam1 (NM\_013591) mouse-tagged ORF clone from OriGene (catalog no. MR226268, Rockville, MD, USA). pLIVE vector, which is designed for liver-specific expression and uses a chimeric promoter composed of the mouse minimal albumin promoter and the mouse alpha fetoprotein enhancer II, was selected to construct the liver-specific Madcam1 overexpression vector.

The gene encoding mouse Madcam1 was amplified from Madcam1 (NM\_013591) mouse tagged ORF clone (pCMV6-Entry-Madcam1) with primers listed below by RT-PCR with OneTaq hot start DNA polymerase (catalog no. M0481, NEB, Ipswich, MA, USA). For more effective expression of Madcam1, Kozak sequences (underlined) were selected and added in forward primer (Madcam1-F-Kozak: 5'-GGCGCGCCGCCACCATGGAATCCATCCTGGCC-3'; Madcam1-R: 5'-CTCGAGTCATAGGTGTGTACATGAGC-3'). The Madcam1 cDNA was then cloned into the AseI and Xho I sites of the pLIVE vector, yielding the pLIVE-Madcam1 plasmid. The large amount of vector DNAs were prepared by an PureLink expi endotoxin-free maxi plasmid purification kit (catalog no. A31231, Invitrogen, Carlsbad, CA, USA) for further hydrodynamic tail vein injection.

#### *Generation of a liver-specific overexpression mouse model*

Six-week-old female WT C57BL/6 mice were purchased from Envigo (Huntingdon, UK). All mice were maintained in a temperature-controlled and pathogen-free environment with 12-hour light–dark cycles with food and water ad libitum. The constructs of pLIVE as a control and pLIVE-Madcam1 vector DNA (250 µg per mouse) were delivered to the mouse liver using the hydrodynamic tail vein injection procedure by using the TransIT-QR hydrodynamic delivery solution (catalog no. MIR 5240, Mirus, Madison, WI, USA) according to the manufacturer's instructions.

#### *Flow cytometry Mouse*

Tumors, mLNs, tLNs, cLNs, ilea, and spleens were harvested at different time points as in-

dicated in the individual experiments. Excised tumors were cut into small pieces and digested in RPMI medium containing Liberase at 25 µg/ml (Roche) and DNaseI at 150 IU/ml (Roche) for 30 min at 37°C, and then crushed and filtered twice using 100-µm and 70-µm cell strainers (Becton & Dickinson). Lymph nodes and spleens were crushed in RPMI medium and subsequently filtered twice through a 100-µm cell strainer. Ileae were collected and fat tissue, Peyer's patches, and feces were removed. Intestines were cut longitudinally and then cut transversally into small pieces into a tube. Pieces were transferred into a new 50-ml tube with 20 ml of IEC washing medium [phosphate-buffered saline (PBS), 5% FCS, 5 mM EDTA, and 1 mM dithiothreitol], vortexed, and shaken at 37°C for 20 min. Tissue and cell suspension were filtered with a cell strainer (100 µm). The filtered cell suspension was discarded. The remaining tissue was incubated for 30 min in LPC medium (RPMI, 5% FCS, 0.25 mg/ml collagenase VIII, and 10 U/ml of DNase I) and then dissociated through a 100-µm cell strainer. The cells obtained from the lamina propria in cell suspension were washed twice with PBS and kept on ice for subsequent analysis. Four million cells from each sample were preincubated with purified anti-mouse CD16/CD32 (clone 93; eBioscience) for 30 min at 4°C before membrane staining. For intracellular staining, the FoxP3 staining kit (eBioscience) was used. Dead cells were excluded using the Live/Dead Fixable Yellow dead cell stain kit (Life Technologies) or LIVE/DEAD Fixable Aqua Dead Cell Stain Kit (Biolegend). For IL-17 and IL-22 staining, cells were stimulated at 37°C during 4 hours with phorbol 12-myristate 13-acetate (PMA)/ionomycin and Golgi stop cocktail. Information on the antibodies used to stain murine cells is found in table S8. Stained samples were acquired on CytoFLEX S 13 colors (Beckman Coulter), and analyses were performed with Kaluza software 2.1 (Beckman Coulter). T<sub>H</sub>17 cell gating depended on the mouse model that was used. The Kaede fluorochrome could not retain its photoconverted state upon fixation with PFA. For Kaede mice, T<sub>H</sub>17 cells were identified as CXCR3<sup>+</sup> and CCR6<sup>+</sup> CD4<sup>+</sup> T cells and T<sub>regs</sub> as CD127<sup>+</sup> CD25<sup>hi</sup> CD4<sup>+</sup> T cells. In other mouse models, T<sub>H</sub>17 and T<sub>reg</sub>17 cells were defined after gating on RORγt<sup>+</sup> CD4<sup>+</sup> or RORγt<sup>+</sup> and/or IL-17A<sup>+</sup> CD25<sup>+</sup> FoxP3<sup>+</sup> CD4<sup>+</sup> cells, respectively.

#### *Human*

Information on the antibodies (clones, sources, and concentrations) used to stain human cells is provided in table S9. For IL-17 and IL-22 staining, cells were stimulated at 37°C for 4 hours with PMA, ionomycin, and brefeldin A (Invitrogen, catalog no. 00-4975). Dead cells were excluded using the LIVE/DEAD Fixable Aqua Dead Cell Stain Kit (Biolegend). Stained

samples were acquired on BD LSRFortessa X-20 Cell Analyzer and analyzed with FlowJo v10.8.1 software.

#### *Immunohistochemistry and quantification of MADCAM-1 in ilea*

Mice ilea “Swiss rolls” were prepared from the experiments and fixed in buffered formalin for 24 to 48 hours and then sent for conventional histological processing. For morphological analysis, hematoxylin, eosin, and saffron staining (HES) slides were generated. Bond Leica automated immunostainer instruments were used to perform immunohistochemistry. Three-micrometer-thick paraffin sections were processed for heat-induced antigen retrieval (ER2 corresponding EDTA buffer, pH 9) for 20 min at 100°C. Slides were incubated with the antibody for 1 hour at room temperature. For MADCAM-1 staining, slides were incubated with MADCAM-1 antibody (Abcam, AP-MAB0842, rat, 1:100) for 1 hour at room temperature. Slides were incubated with a Polink rat kit as secondary antibodies and revealed with di-amino-benzidine-peroxidase (DAB, ThermoFisher, ready for use solution, 1 ml), after incubation for 5 min at room temperature.

For image analysis and MADCAM-1 quantification, QuPath software was used (87). ROIs were defined first by “simple tissue detection” function and modified by hand in each whole slide image (WSI). To quantify the cell density of biomarker-positive cells, “Positive cell detection” was used.

#### *Histological processing of MADCAM-1-expressing liver*

Murine livers were obtained from the experiments and fixed in buffered formalin for 24–48 hours and then cut vertically in parallel sections, which were sent for conventional histological processing. For morphological analysis, hematoxylin, eosin, and saffron staining (HES) slides were generated. Bond Leica automated immunostainer instruments were used to perform immunohistochemistry. Three-micrometer-thick paraffin sections were processed for heat-induced antigen retrieval (ER2 corresponding EDTA buffer, pH 9) for 20 min at 100°C. Slides were incubated with the antibody for 1 hour at room temperature. The following antibodies were used: anti-FoxP3 (Cell Signaling Technology, D608R, rabbit, 1:200, ER2) and anti-RORγt (Abcam, EPR20006, rabbit, 1:3000, ER2). The antibodies were detected with DAB (ThermoFisher, ready-for-use solution, 1 ml), after incubation for 5 min at room temperature. Finally, the sections were counterstained by hematoxylin (Leica Biosystems).

#### *Quantification of FoxP3 and MADCAM-1 in MADCAM-1-expressing liver*

Images for analysis were acquired as WSIs with a slide scanner (Zeiss Axio Scan.Z1) and

Olympus VS120 whole-slide imaging system. Image analysis was performed using QuPath, version 0.3.2 (87). WSI for FoxP3 were evaluated through multiple steps: (i) simple tissue detection was performed (threshold 220, requested pixel size 20  $\mu\text{m}$ , minimum area 100,000  $\mu\text{m}^2$ , max fill area 100,000  $\mu\text{m}^2$ , smooth image, cleanup with median filter, smooth coordinates, single annotation); (ii) fast cell counts (cell detection channel DAB, Gaussian sigma 1.5  $\mu\text{m}$ , background radius 15  $\mu\text{m}$ , use difference of Gaussians, cell detection threshold 0.5, DAB threshold 0.5); (iii) exclusion of detections corresponding to artifacts (folded tissue, dark pigment sedimented, hemorrhage, intravascular lymphocytes) was performed by a pathologist (L.L.); (iv) create density map; and (v) select the region of interest (ROI) with 1  $\text{mm}^2$ , representing the highest density in the tissue (hotspot). Hotspot density was then normalized for each experiment based on the control group, and then pooled ( $n = 2$ ). WSIs for ROR $\gamma$ t were evaluated for hotspot compared with the same ROI as indicated for FoxP3. The ROR $\gamma$ t<sup>+</sup> nuclei were then counted manually, based on morphology, because many nuclei from hepatocytes were also stained in some of the evaluated conditions.

#### Tracing migration of leukocytes from the gut to the TME

##### Kaede experiments

Kaede transgenic mice were anesthetized with 2 to 2.5% isoflurane and administered buprenorphine (0.01 mg/kg body weight) intraperitoneally for analgesia. For photoconversion of ilea, abdominal skin and peritoneum were cut at the midline to access the intraperitoneal terminal ileum. For photoconversion of the cecum, ileum, and mLNs, the cecal pole was first identified. Then, the cecal pole, including the terminal ileum, the mLNs, and proximal colon, was gently mobilized through the mid-abdominal incision onto a sterile plastic-coated surgical drape. Nontarget structures were covered with aluminum foil. The ventral and dorsal parts of the targeted structures were exposed to ultraviolet light emitted from a 395-nm wavelength emitting diode (Winzvon) light for 30 s each. After illumination, the tissue was moistened with sterile isotonic sodium chloride and gently repositioned into the peritoneal cavity. The peritoneal membrane was closed by continuous stitch with a 5-0 monofil nylon suture (Ethicon). The skin was closed with two 9-mm wound clips (EZ Clip Kit).

#### CFSE staining of mLN cells up to TME or tdLNs

C57BL/6 mice were anesthetized with 2 to 2.5% isoflurane and administered buprenorphine (0.01 mg/kg body weight) intraperitoneally for analgesia. Abdominal skin and

peritoneum were cut at the midline to access the mLNs. The mLNs were gently mobilized through the midabdominal incision onto a sterile plastic-coated surgical drape. Ileum draining mLNs were visually identified according to their vasculature. The two most prominent mLNs were injected with 100  $\mu\text{M}$  CFSE diluted in 5  $\mu\text{l}$  of PBS using a 30-Ga insulin syringe. After repositioning the mLNs, the peritoneal membrane was closed by continuous stitch with a 5-0 monofil nylon suture (Ethicon).

#### RNA extraction and RT-qPCR

Lysis and extraction protocols were identical for human and mouse samples. Tumor or intestinal samples were snap-frozen in liquid nitrogen in RLT Plus buffer containing 0.1% beta mercaptoethanol. On the day of extraction, samples were thawed at 4°C and homogenized in a microtube homogenizer (Benchmark Scientific) in RNA-free glass bead tubes (Dutscher). Total RNA extraction and genomic DNA removal were performed with the RNeasy Mini kit (Qiagen) following the manufacturer's recommendations. A maximum of 1  $\mu\text{g}$  of RNA, measured using a NanoDrop Spectrophotometer (ThermoFisher Scientific), was reverse-transcribed into cDNA with a mixture composed of SuperScript III Reverse Transcriptase (Life Technologies), RNaseOUT<sup>TM</sup> Recombinant Ribonuclease Inhibitor (Life Technologies), random primers (Promega), and Deoxynucleoside Triphosphate Set, PCR grade (Roche Diagnostics).

#### Quantitative gene expression assay

The expression of mouse and human *B2M*, *FOXP3*, *IFNG*, *IL10*, *IL17A*, *IL22*, *MADCAM1*, *VCAM1*, *PPIA*, *RORC*, *IL18*, and *TBX21* genes (all from Life Technologies) was analyzed with the TaqMan Gene Expression Assay using the Universal Master Mix II on a StepOnePlus Real-Time PCR System (Life Technologies). Amplifications were performed using the following ramping profile: one cycle at 95°C for 10 min, followed by 45 cycles of 95°C for 30 s, and 60°C for 1 min. RT-qPCR data were normalized to the expression levels of the housekeeping genes *B2M* or *Ppia*, as indicated in each figure, by means of the  $2^{-\Delta\text{Ct}}$  method multiplied by  $10^6$ .

#### Tissue lysis and chemokine analyses

Intestinal and tumoral samples were snap-frozen in liquid nitrogen in a nondenaturing cell lysis buffer containing 50 mM Tris HCl, pH 7.4, 150 mM NaCl, 300 mM sucrose, 10 mM EDTA, 0.1% Triton X-100, and Complete, Mini, EDTA-free Protease Inhibitor Cocktail (Roche). For subsequent lysis, samples were thawed at 4°C and lysed on a tube homogenizer (Precellys) in ceramic beads lysis tubes (Precellys). Tissue homogenate was centrifuged at 4000g for 5 min. The supernatant was used for sub-

sequent analysis. Chemokine concentrations in the tissue lysate were determined according to the manufacturer's recommendations using the CCL2, CCL3, CCL4, CCL5, CCL25, and MAdCAM-1 DuoSet ELISA kits (R&D Systems) or using Legendplex Mouse proinflammatory chemokine panel (BioLegend) with cytometric analysis performed on a CytoFLEX S (Beckman Coulter).

#### Ileal tissue sample preparation and bile acid detection by UHPLC-MS

Approximately 30 mg of collected tissue was weighed and placed in a 2-ml homogenizer tube with ceramic beads (Precellys, Bertin Technologies, France) with 1 ml of ice-cold extraction mixture (9:1 methanol–water, –20°C, with labeled <sup>13</sup>C-glycocholic acid as internal standard). To facilitate the extraction of endogenous metabolites, samples were then completely homogenized (3 cycles of 20 s/2380g; Precellys 24, Bertin Technologies, Montigny-le Bretonneux, France) and centrifuged (10 min at 15,000g, 4°C). To detect bile acids, 300  $\mu\text{l}$  of supernatant was collected and treated following a previously described protocol (82). Bile acids were analyzed by LC-MRM (Multiple Reaction Monitoring) with a 1290 UHPLC (Ultra-High Performance Liquid Chromatography, Agilent Technologies) coupled to a mass spectrometer 6470 TQ (Triple Quadrupole, Agilent Technologies), as previously described (83). Targeted data were cleaned with a R (version 4.0) dedicated package (<https://github.com/kroemerlab/GRMeta>).

#### Bulk RNA sequencing of $\alpha 4\beta 7^{-/-}$ CD4<sup>+</sup> mesenteric T cells

$\alpha 4\beta 7^{+}$  and  $\alpha 4\beta 7^{-}$  CD4<sup>+</sup> T cells were isolated from mLNs by flow cytometry. Preparation of mRNA-seq libraries and nextseq 75SE run deep sequencing were performed at GeneCore EMBL (Heidelberg, Germany).

#### Single-cell RNA sequencing by BD Rhapsody

After isolation of CFSE<sup>+</sup> CD4<sup>+</sup> T cells by flow cytometry, 10,000 cells were washed in cold PBS and loaded onto a BD Rhapsody cartridge and processed according to the manufacturer's instructions for targeted single-cell RNA-seq using the predesigned Immune Response Panel (Mouse). The library was clustered at 1.75 pM on a NextSeq500 system (Illumina) to generate ~40,000 paired-end reads per cell using High Output v2 chemistry. Sequenced single-cell data was demultiplexed using bcl2fastq2 v2.20.

#### Single-cell TCR and RNA library construction and sequencing by 10X Genomics Chromium

After isolation of CFSE<sup>+</sup>CD4<sup>+</sup> and CD8<sup>+</sup> T cell by flow cytometry from mLNs, cLNs, tdLNs, and tumors, single-cell-library construction was performed using Chromium Next GEM

Single Cell 5' Kit v2 (PN-1000263), Chromium Next GEM Chip K Single Cell Kit (PN-1000287), Single Cell VDJ 5' Gel Bead, Chromium Single Cell Mouse TCR Amplification Kit, 16 rxns (reactions) (PN-1000254), Library Construction Kit (16 rxns) (PN-1000190), and Dual Index Kit TT Set A (96 rxns) (PN-1000215) kits according to the manufacturer's protocol. Briefly, single-cell suspensions from a total of 500 to 20,000 cells with barcoded gel beads and partitioning oil were loaded to Chromium Next GEM Chip K to generate single-cell gel bead-in-emulsion. Full-length cDNA along with cell barcode identifiers were PCR-amplified to generate 5'Gene Expression (GEX) libraries and V(D)J libraries. Libraries were sequenced using a NovaSeq 6000 (Illumina) to achieve a minimum of 23,000 paired-end reads per cell for GEX and 7000 paired-end reads per cell for V(D)J. Reads were aligned using Cell Ranger v6.1.1 to the GRCh38 mouse references.

### Repertoire clonality

TCR sequencing data were processed using the "immunarch" R package. Clonotypes within each population and compartments were then divided into fractions with an occurrence of 1 or >1. The cumulative frequency of each fraction was calculated within the repertoire of each sample.

### Sequence similarity analysis

DeepTCR was used to cluster paired TRA-TRB clonotypes on the basis of sequence similarity, using a train variational autoencoder. This generates clusters composed of sequences with a likelihood of shared specificities. The clusters were assigned as being mLN, tumor/dLN or shared based on the percentage of clonotypes composing them. A cluster was considered as specific to a compartment if the log2 fold change (FC) was equal to or higher than 1.5. Otherwise, clusters were considered as shared between the compartments (52).

### Single-cell RNA-seq analysis

Expression matrices were analyzed using the R environment (version 4.2.1) with the Seurat package (v4.2.1). High-quality cells characterized by <10% of mitochondrial genes, >200 unique molecular identifier (UMI) features, and <15,000 unique UMIs were selected for further analysis. Count matrix was normalized with regularized negative binomial regression based on the 3000 most variable genes using the SCTransform function. Principal component analysis was used for dimensionality reduction using the RunPCA on the 3000 most variable genes. Contributive components were identified visually using an elbow plot. Nearest neighbors were determined with the FindNeighbors function using contributive PCA components, and cells were clustered using the Louvain clustering algorithm

with the FindClusters function. Resolution of the clustering algorithm was chosen based on a bootstrapping procedure, the resolution giving rise to the maximum number of clusters with co-assignment probabilities superior to 5% was chosen. Differential gene expression analysis was performed using the FindMarkers function and *P* values were corrected using the p.adj base function with the FDR procedure. Volcano plot visualization was performed using the ggplot2(v3.4.0) R package, Heatmap visualization was performed using the ComplexHeatmap (v2.14.0) R package, and Venn Diagram visualization was performed using the gvenv R package (v0.1.9).

### Cell lines and treatment

Culture media and supplements for cell culture were obtained from Life Technologies (Carlsbad, CA, USA), and plastic material was obtained from Greiner BioOne (Kremsmünster, Austria) and Corning (Corning, New York, USA). Mouse TSECs were a generous gift from B. P. Fennimore (University of Colorado Anschutz Medical Campus, Aurora, CO, USA) and bEnd.3 cells were purchased from the ATCC. TSECs were cultured in Dulbecco's modified Eagle's medium/nutrient mixture F-12 (DMEM/F-12) plus endothelial growth supplement (catalog no. 1052, ScienCell, Carlsbad, CA, USA), supplemented with 10% fetal bovine serum (FBS), 10 U/ml of penicillin sodium, and 10 µg/ml of streptomycin sulfate. bEnd.3 cells were cultured in DMEM with 2.5 mM L-glutamine, supplemented with 10% FBS, 10 U/ml penicillin sodium, and 10 µg/ml of streptomycin sulfate. Both cell lines were cultured in the presence of 5% CO<sub>2</sub> at 37°C. Transfected TSECs (TSEC::MAdCAM-1-GFP) and bEnd.3 cells (bEnd.3::MAdCAM-1-GFP) were selected with 500 µg/ml G418 sulfate (50 mg/ml, catalog no. 10131027, Gibco), and stable transformants were maintained under G418 selection pressure. Recombinant murine TNF-α (catalog no. 315-01A, PeproTech) and IL-1β (catalog no. 211-11B, PeproTech) were diluted in culture media from a stock of 40 µg/ml at the time of treatment. Bile acids (lithocholic acid (LCA) (catalog no. 700218P-10MG, Sigma-Aldrich), dehydrolithocholic acid (3-oxo-LCA) (catalog no. 700217P-10MG, Sigma-Aldrich), allolithocholic acid (allo-LCA) (catalog no. 700330P-5MG, Sigma-Aldrich), isoallo-LCA (catalog no. R203424-1MG, Sigma-Aldrich), tauroolithocholic acid sodium salt (tauro-LCA) (catalog no. 700252P-10MG, Sigma-Aldrich), sodium chenodeoxycholate (CDCA) (catalog no. C8261-1G, Sigma-Aldrich), sodium taurochenodeoxycholate (TCDCA) (catalog no. T6260-100MG, Sigma-Aldrich), deoxycholic acid (DCA) (catalog no. 30960-25G, Sigma-Aldrich), UDCA (catalog no. 208590250, Thermoscientific), tauroursodeoxycholic acid (TUDCA) (catalog no. 580549-1GM, Millipore), glycooursodeoxy-

cholic acid (GUDCA) (catalog no. 06863-1G, Sigma-Aldrich), and taurodeoxycholic acid (TDCA) (catalog no. 580221-5GM, Millipore) and FXR agonists/antagonists (GW4064 (catalog no. G5172-5MG, Sigma-Aldrich), cilofexor (catalog no. HY-109083, MCE), tropifexor (catalog no. HY-107418, MedChemExpress (MCE), and (Z)-guggulsterone (catalog no. G5168-25MG, Sigma-Aldrich)) dissolved in DMSO were diluted 1:1000, 1:10,000, and 1:100,000 in culture media to a final concentration of 100 µM, 10 µM, and 1 µM, respectively. Bacteria were cultured (and in some instances pasteurized) before being diluted in culture media to a working concentration with an optical density of 0.5, 0.25, and 0.1, respectively (*Akk. p2261* everImmune strain, *E. clostridioformis*).

### Construction of MAdCAM-1 promoter plasmid

The MAdCAM-1 promoter construct is a PCR product from mouse genomic DNA amplified using 5'-GGAATTCTACCCCCACAGGCTGCC-3' as forward primer (EcoRI site is underlined, Eurofins, Nantes, France) and 5'-AGGCCGCGGGGGCCGCGAGCTTCTCTAC-3' as the reverse primer (SacII site is underlined, Eurofins). After digestion by EcoRI-HF and SacII (NEB, Ipswich, MA, USA), the MAdCAM-1 promoter DNA fragment was extracted using a Monarch DNA gel extraction kit (NEB, Ipswich, MA, USA). The purified fragments were subcloned into the promoterless pAcGFP1-1 vector (Clontech, Mountain View, CA, USA).

### Establishment of MAdCAM-1 promoter reporter cell lines

TSECs and bEnd.3 cells were transfected with the recombinant expression vector pAcGFP1-1-MAdCAM-1 using FuGENE HD transfection reagent (catalog no. E2312, Promega). Twenty-four hours after transfection, stable transfectants were isolated by selection with 500 µg/ml G418. The transfectants (TSEC::MAdCAM-1-GFP and bEnd.3::MAdCAM-1-GFP) were maintained in culture medium containing 500 µg/ml of G418 for 2 weeks. The G418-resistant cells were selected and single-cell clones were isolated to establish TSEC::MAdCAM-1-GFP and bEnd.3::MAdCAM-1-GFP stable cell lines expressing GFP under the control of the MAdCAM-1 promoter.

### High-content microscopy

TSEC::MAdCAM-1-GFP and bEnd.3::MAdCAM-1-GFP cells were seeded in 384-well/96-well µclear imaging plates (Greiner BioOne) and allowed to adapt overnight. Cells were treated with the indicated agents, then fixed with 3.7% PFA (w/v in PBS) (catalog no. F8775, Sigma-Aldrich) containing 2 µg/ml of Hoechst 33342 at 4°C overnight. Subsequently, the fixative was exchanged with PBS and the plates were analyzed by automated microscopy. Image acquisition was performed using an ImageXpress



Micro C automated confocal microscope (Molecular Devices, Sunnyvale, California, USA) equipped with a 20× PlanApo objective (Nikon, Tokyo, Japan), followed by automated image processing with R software using the EBImage package (available from the Bioconductor repository <https://www.bioconductor.org>) and the MorphR package (available from the GitHub repository <https://github.com/kroemerlab/MorphR>). In short, cytoplasm and nucleus were segmented and fluorescence intensities were assessed. After exclusion of cellular debris and dead cells, data were normalized, statistically evaluated, and graphically depicted. Images were also extracted and pixel intensities scaled (to the same extent for all images of a given experiment) using R software. At least four view fields were analyzed per well, and each experiment was assessed at least four times.

## Statistics

### *In vitro and in vivo*

Data analyses were performed either with the statistical environment R (<http://www.R-project.org/>) or Prism 6 (GraphPad, San Diego, CA, USA). The standardization of each marker was performed using the *z* score (difference of each sample value from the mean and/or standard deviation). When a control group was available, the data were standardized by dividing the value by the mean of the control group. Nonparametric Mann-Whitney *U* test was used for comparison of two unpaired groups. The Wilcoxon matched-pairs signed-rank test was used to compare two groups of paired samples. Kruskal-Wallis *H* test was used to compare more than two groups, correcting the statistical significance for multiple comparisons and FDR using the two-stage step-up method of Benjamini, Krieger, and Yekutieli. All reported tests are two-tailed and were considered significant at  $P < 0.05$ .

## Patients

sMAdCAM-1 was a prognostic factor of the patient response in NSCLC, renal cell carcinoma, and bladder cancer patients. For each cohort, two groups of patients were defined by the sMAdCAM-1 median. Overall survival and progression-free survival analyses were performed using the Kaplan-Meier estimator, and the patient groups were compared using the log-rank (Mantel-Cox) test.

## REFERENCES AND NOTES

1. C. Robert *et al.*, Ipilimumab plus dacarbazine for previously untreated metastatic melanoma. *N. Engl. J. Med.* **364**, 2517–2526 (2011). doi: [10.1056/NEJMoa1104621](https://doi.org/10.1056/NEJMoa1104621); pmid: 21639810
2. J. Brahmer *et al.*, Nivolumab versus docetaxel in advanced squamous-cell non-small-cell lung cancer. *N. Engl. J. Med.* **373**, 123–135 (2015). doi: [10.1056/NEJMoa1504627](https://doi.org/10.1056/NEJMoa1504627); pmid: 26028407
3. S. Spranger, R. Bao, T. F. Gajewski, Melanoma-intrinsic  $\beta$ -catenin signalling prevents anti-tumour immunity. *Nature* **523**, 231–235 (2015). doi: [10.1038/nature14404](https://doi.org/10.1038/nature14404); pmid: 25970248
4. J. Gao *et al.*, Loss of IFN- $\gamma$  pathway genes in tumor cells as a mechanism of resistance to anti-CTLA-4 therapy. *Cell* **167**, 397–404.e9 (2016). doi: [10.1016/j.cell.2016.08.069](https://doi.org/10.1016/j.cell.2016.08.069); pmid: 27667683
5. N. J. Neubert *et al.*, T cell-induced CSF1 promotes melanoma resistance to PD1 blockade. *Sci. Transl. Med.* **10**, eaan3311 (2018). doi: [10.1126/scitranslmed.aan3311](https://doi.org/10.1126/scitranslmed.aan3311); pmid: 29643229
6. A. Elkrief, L. Derosa, G. Kroemer, L. Zitvogel, B. Routy, The negative impact of antibiotics on outcomes in cancer patients treated with immunotherapy: A new independent prognostic factor? *Ann. Oncol.* **30**, 1572–1579 (2019). doi: [10.1093/annonc/mdz206](https://doi.org/10.1093/annonc/mdz206); pmid: 31268133
7. B. Routy *et al.*, Gut microbiome influences efficacy of PD-1-based immunotherapy against epithelial tumors. *Science* **359**, 91–97 (2018). doi: [10.1126/science.aan3706](https://doi.org/10.1126/science.aan3706); pmid: 29097494
8. J. J. Mohiuddin *et al.*, Association of antibiotic exposure with survival and toxicity in patients with melanoma receiving immunotherapy. *J. Natl. Cancer Inst.* **113**, 162–170 (2021). doi: [10.1093/jnci/djaa057](https://doi.org/10.1093/jnci/djaa057); pmid: 32294209
9. L. Derosa *et al.*, Microbiota-centered interventions: The next breakthrough in immuno-oncology? *Cancer Discov.* **11**, 2396–2412 (2021). doi: [10.1158/2159-8290.CD-21-0236](https://doi.org/10.1158/2159-8290.CD-21-0236); pmid: 34400407
10. L. Derosa *et al.*, Intestinal *Akkermansia muciniphila* predicts clinical response to PD-1 blockade in advanced non-small cell lung cancer patients. *Nat. Med.* **28**, 315–324 (2022). doi: [10.1038/s41591-021-01655-5](https://doi.org/10.1038/s41591-021-01655-5); pmid: 35115705
11. L. Derosa *et al.*, Gut bacteria composition drives primary resistance to cancer immunotherapy in renal cell carcinoma patients. *Eur. Urol.* **78**, 195–206 (2020). doi: [10.1016/j.eururo.2020.04.044](https://doi.org/10.1016/j.eururo.2020.04.044); pmid: 32376136
12. G. Gorfu, J. Rivera-Nieves, K. Ley, Role of  $\beta$ 7 integrins in intestinal lymphocyte homing and retention. *Curr. Mol. Med.* **9**, 836–850 (2009). doi: [10.2174/156652409789105525](https://doi.org/10.2174/156652409789105525); pmid: 19860663
13. M. Briskin *et al.*, Human mucosal addressin cell adhesion molecule-1 is preferentially expressed in intestinal tract and associated lymphoid tissue. *Am. J. Pathol.* **151**, 97–110 (1997). doi: [10.1016/j.ajcp.00406.2003](https://doi.org/10.1016/j.ajcp.00406.2003); pmid: 15483224
14. H. Ogawa *et al.*, Mechanisms of MAdCAM-1 gene expression in human intestinal microvascular endothelial cells. *Am. J. Physiol. Cell Physiol.* **288**, C272–C281 (2005). doi: [10.1152/ajpcell.00406.2003](https://doi.org/10.1152/ajpcell.00406.2003); pmid: 15483224
15. B. G. Feagan *et al.*, Vedolizumab as induction and maintenance therapy for ulcerative colitis. *N. Engl. J. Med.* **369**, 699–710 (2013). doi: [10.1056/NEJMoa1215734](https://doi.org/10.1056/NEJMoa1215734); pmid: 23964932
16. M. Hassan-Zahraee *et al.*, Anti-MAdCAM antibody increases  $\beta$ 7 + T cells and CCR9 gene expression in the peripheral blood of patients with Crohn's disease. *J. Crohns Colitis* **12**, 77–86 (2018). doi: [10.1093/ecco-jcc/jjx121](https://doi.org/10.1093/ecco-jcc/jjx121); pmid: 28961803
17. W. Reinisch *et al.*, Long-term safety and efficacy of the anti-MAdCAM-1 monoclonal antibody ontamalizumab [SHP647] for the treatment of ulcerative colitis: The open-label study TURANDOT II. *J. Crohns Colitis* **15**, 938–949 (2021). doi: [10.1093/ecco-jcc/jjab023](https://doi.org/10.1093/ecco-jcc/jjab023); pmid: 33599720
18. D. R. Littman, A. Y. Rudensky, Th17 and regulatory T cells in mediating and restraining inflammation. *Cell* **140**, 845–858 (2010). doi: [10.1016/j.cell.2010.02.021](https://doi.org/10.1016/j.cell.2010.02.021); pmid: 20303875
19. P. Pandiyan *et al.*, Microbiome dependent regulation of Tregs and Th17 cells in mucosa. *Front. Immunol.* **10**, 426 (2019). doi: [10.3389/fimmu.2019.00426](https://doi.org/10.3389/fimmu.2019.00426); pmid: 30906299
20. C. F. Krebs *et al.*, Autoimmune renal disease is exacerbated by SIP-receptor-1-dependent intestinal Th17 cell migration to the kidney. *Immunity* **45**, 1078–1092 (2016). doi: [10.1016/j.immuni.2016.10.020](https://doi.org/10.1016/j.immuni.2016.10.020); pmid: 27851911
21. Y. K. Lee, J. S. Menezes, Y. Umesaki, S. K. Mazmanian, Proinflammatory T-cell responses to gut microbiota promote experimental autoimmune encephalomyelitis. *Proc. Natl. Acad. Sci. U.S.A.* **108** (Suppl 1), 4615–4622 (2011). doi: [10.1073/pnas.1000082107](https://doi.org/10.1073/pnas.1000082107); pmid: 20660719
22. A. M. Magnuson *et al.*, Population dynamics of islet-infiltrating cells in autoimmune diabetes. *Proc. Natl. Acad. Sci. U.S.A.* **112**, 1511–1516 (2015). doi: [10.1073/pnas.1423769112](https://doi.org/10.1073/pnas.1423769112); pmid: 25605891
23. A. M. Morton *et al.*, Endoscopic photoconversion reveals unexpectedly broad leukocyte trafficking to and from the gut. *Proc. Natl. Acad. Sci. U.S.A.* **111**, 6696–6701 (2014). doi: [10.1073/pnas.1405634111](https://doi.org/10.1073/pnas.1405634111); pmid: 24753589
24. H.-J. Wu *et al.*, Gut-residing segmented filamentous bacteria drive autoimmune arthritis via T helper 17 cells. *Immunity* **32**, 815–827 (2010). doi: [10.1016/j.immuni.2010.06.001](https://doi.org/10.1016/j.immuni.2010.06.001); pmid: 20620945
25. M. R. I. Young, Th17 cells in protection from tumor or promotion of tumor progression. *J. Clin. Cell. Immunol.* **7**, 431 (2016). doi: [10.4172/2155-9899.1000431](https://doi.org/10.4172/2155-9899.1000431); pmid: 27453801
26. E. Sefik *et al.*, MUCOSAL IMMUNOLOGY. Individual intestinal symbionts induce a distinct population of ROR $\gamma^+$  regulatory T cells. *Science* **349**, 993–997 (2015). doi: [10.1126/science.aaa9420](https://doi.org/10.1126/science.aaa9420); pmid: 26272906
27. N. R. Blatner *et al.*, Expression of ROR $\gamma$ t marks a pathogenic regulatory T cell subset in human colon cancer. *Sci. Transl. Med.* **4**, 164ra159 (2012). doi: [10.1126/scitranslmed.3004566](https://doi.org/10.1126/scitranslmed.3004566); pmid: 23241743
28. A. Rizzo *et al.*, ROR $\gamma$ t-expressing Tregs drive the growth of colitis-associated colorectal cancer by controlling IL6 in dendritic cells. *Cancer Immunol. Res.* **6**, 1082–1092 (2018). doi: [10.1158/2326-6066.CIR-17-0698](https://doi.org/10.1158/2326-6066.CIR-17-0698); pmid: 29991500
29. K. N. Haas, J. L. Blanchard, Reclassification of the *Clostridium claudii* and *Clostridium sphenoides* clades as *Enterocloster* gen. nov. and *Lacrimispora* gen. nov., including reclassification of 15 taxa. *Int. J. Syst. Evol. Microbiol.* **70**, 23–34 (2020). doi: [10.1099/ijsem.0.003698](https://doi.org/10.1099/ijsem.0.003698); pmid: 31782700
30. R. Gacesa *et al.*, Environmental factors shaping the gut microbiome in a Dutch population. *Nature* **604**, 732–739 (2022). doi: [10.1038/s41586-022-04567-7](https://doi.org/10.1038/s41586-022-04567-7); pmid: 35418674
31. S. Yonekura *et al.*, Cancer induces a stress ileopathy depending on  $\beta$ -adrenergic receptors and promoting dysbiosis that contributes to carcinogenesis. *Cancer Discov.* **12**, 1128–1151 (2022). doi: [10.1158/2159-8290.CD-21-0999](https://doi.org/10.1158/2159-8290.CD-21-0999); pmid: 34930787
32. A.-G. Goubet *et al.*, Multifaceted modes of action of the anticancer probiotic *Enterococcus hirae*. *Cell Death Differ.* **28**, 2276–2295 (2021). doi: [10.1038/s41418-021-00753-8](https://doi.org/10.1038/s41418-021-00753-8); pmid: 33976389
33. E. N. Baruch *et al.*, Fecal microbiota transplant promotes response in immunotherapy-refractory melanoma patients. *Science* **371**, 602–609 (2021). doi: [10.1126/science.abb5920](https://doi.org/10.1126/science.abb5920); pmid: 33303685
34. D. Davar *et al.*, Fecal microbiota transplant overcomes resistance to anti-PD-1 therapy in melanoma patients. *Science* **371**, 595–602 (2021). doi: [10.1126/science.abb3363](https://doi.org/10.1126/science.abb3363); pmid: 33542131
35. B. Routy *et al.*, The gut microbiota influences anticancer immunosurveillance and general health. *Nat. Rev. Clin. Oncol.* **15**, 382–396 (2018). doi: [10.1038/s41571-018-0006-2](https://doi.org/10.1038/s41571-018-0006-2); pmid: 29636538
36. R. Y. Gao *et al.*, Bile acids modulate colonic MAdCAM-1 expression in a murine model of combined cholestasis and colitis. *Mucosal Immunol.* **14**, 479–490 (2021). doi: [10.1038/s41385-020-00347-6](https://doi.org/10.1038/s41385-020-00347-6); pmid: 33004979
37. D. V. Guziro, R. A. Quinn, Review: Microbial transformations of human bile acids. *Microbiome* **9**, 140 (2021). doi: [10.1186/s40168-021-01101-1](https://doi.org/10.1186/s40168-021-01101-1); pmid: 34127070
38. Y. Sato *et al.*, Novel bile acid biosynthetic pathways are enriched in the microbiome of centenarians. *Nature* **599**, 458–464 (2021). doi: [10.1038/s41586-021-03832-5](https://doi.org/10.1038/s41586-021-03832-5); pmid: 34325466
39. J. B. J. Ward *et al.*, Ursodeoxycholic acid and lithocholic acid exert anti-inflammatory actions in the colon. *Am. J. Physiol. Gastrointest. Liver Physiol.* **312**, G550–G558 (2017). doi: [10.1152/ajpgi.00256.2016](https://doi.org/10.1152/ajpgi.00256.2016); pmid: 28360029
40. M. Tomura *et al.*, Monitoring cellular movement in vivo with photoconvertible fluorescence protein “Kaede” transgenic mice. *Proc. Natl. Acad. Sci. U.S.A.* **105**, 10871–10876 (2008). doi: [10.1073/pnas.0802278105](https://doi.org/10.1073/pnas.0802278105); pmid: 18663225
41. V. Singh *et al.*, Microbiota dysbiosis controls the neuroinflammatory response after stroke. *J. Neurosci.* **36**, 7428–7440 (2016). doi: [10.1523/JNEUROSCI.1114-16.2016](https://doi.org/10.1523/JNEUROSCI.1114-16.2016); pmid: 27413153
42. C. M. Rini *et al.*, A novel endothelial L-selectin ligand activity in lymph node medulla that is regulated by alpha(L3)-fucosyltransferase-IV. *J. Exp. Med.* **198**, 1301–1312 (2003). doi: [10.1084/jem.20030182](https://doi.org/10.1084/jem.20030182); pmid: 14597733
43. J. Mitoma *et al.*, Critical functions of N-glycans in L-selectin-mediated lymphocyte homing and recruitment. *Nat. Immunol.* **8**, 409–418 (2007). doi: [10.1038/ni1442](https://doi.org/10.1038/ni1442); pmid: 17334369
44. E. Cano-Gamez *et al.*, Single-cell transcriptomics identifies an effectormess gradient shaping the response of CD4 $^{+}$  T cells to cytokines. *Nat. Commun.* **11**, 1801 (2020). doi: [10.1038/s41467-020-15543-y](https://doi.org/10.1038/s41467-020-15543-y); pmid: 32286271
45. Z. T. Freeman *et al.*, A conserved intratumoral regulatory T cell signature identifies 4-1BB as a pan-cancer target. *J. Clin. Invest.* **130**, 1405–1416 (2020). doi: [10.1172/JCI128672](https://doi.org/10.1172/JCI128672); pmid: 32015231
46. Y. Gao *et al.*, Transcriptional profiling identifies caspase-1 as a T cell-intrinsic regulator of Th17 differentiation. *J. Exp. Med.* **217**, e20190476 (2020). doi: [10.1084/jem.20190476](https://doi.org/10.1084/jem.20190476); pmid: 31967646
47. D. Lu *et al.*, The phosphatase PAC1 acts as a T cell suppressor and attenuates host antitumor immunity. *Nat. Immunol.* **21**, 287–297 (2020). doi: [10.1038/s41590-019-0577-9](https://doi.org/10.1038/s41590-019-0577-9); pmid: 31932812
48. J.-H. Kim *et al.*, Molecular networks of FOXP family: Dual biologic functions, interplay with other molecules and clinical implications in cancer progression. *Mol. Cancer* **18**, 180 (2019). doi: [10.1186/s12943-019-1110-3](https://doi.org/10.1186/s12943-019-1110-3); pmid: 31815635

49. L. Li, N. Patsoukis, V. Petkova, V. A. Boussiotis, Runx1 and Runx3 are involved in the generation and function of highly suppressive IL-17-producing T regulatory cells. *PLOS ONE* **7**, e45115 (2012). doi: [10.1371/journal.pone.0045115](https://doi.org/10.1371/journal.pone.0045115); pmid: [22984619](https://pubmed.ncbi.nlm.nih.gov/22984619/)
50. L. Belariff *et al.*, IL-7 receptor influences anti-TNF responsiveness and T cell gut homing in inflammatory bowel disease. *J. Clin. Invest.* **129**, 1910–1925 (2019). doi: [10.1172/JCI121668](https://doi.org/10.1172/JCI121668); pmid: [30939120](https://pubmed.ncbi.nlm.nih.gov/30939120/)
51. Y. Chen *et al.*, Pik3ip1 is a negative immune regulator that inhibits antitumor T-cell immunity. *Clin. Cancer Res.* **25**, 6180–6194 (2019). doi: [10.1158/1078-0432.CCR-18-4134](https://doi.org/10.1158/1078-0432.CCR-18-4134); pmid: [31350312](https://pubmed.ncbi.nlm.nih.gov/31350312/)
52. J.-W. Sidhom, H. B. Larman, D. M. Pardoll, A. S. Baras, Author Correction: DeepTCR is a deep learning framework for revealing sequence concepts within T-cell repertoires. *Nat. Commun.* **12**, 2309 (2021). doi: [10.1038/s41467-021-22667-2](https://doi.org/10.1038/s41467-021-22667-2); pmid: [33850137](https://pubmed.ncbi.nlm.nih.gov/33850137/)
53. T. C. Wirth *et al.*, Repetitive antigen stimulation induces stepwise transcriptional diversification but preserves a core signature of memory CD8(+) T cell differentiation. *Immunity* **33**, 128–140 (2010). doi: [10.1016/j.immuni.2010.06.014](https://doi.org/10.1016/j.immuni.2010.06.014); pmid: [20619696](https://pubmed.ncbi.nlm.nih.gov/20619696/)
54. T. Wu *et al.*, The TCF1-Bcl6 axis counteracts type I interferon to repress exhaustion and maintain T cell stemness. *Sci. Immunol.* **1**, eaa8593 (2016). doi: [10.1126/sciimmunol.aai8593](https://doi.org/10.1126/sciimmunol.aai8593); pmid: [28018990](https://pubmed.ncbi.nlm.nih.gov/28018990/)
55. E. J. Wherry *et al.*, Molecular signature of CD8+ T cell exhaustion during chronic viral infection. *Immunity* **27**, 670–684 (2007). doi: [10.1016/j.immuni.2007.09.006](https://doi.org/10.1016/j.immuni.2007.09.006); pmid: [17950003](https://pubmed.ncbi.nlm.nih.gov/17950003/)
56. K. Araki *et al.*, Translation is actively regulated during the differentiation of CD8<sup>+</sup> effector T cells. *Nat. Immunol.* **18**, 1046–1057 (2017). doi: [10.1038/ni.3795](https://doi.org/10.1038/ni.3795); pmid: [28714979](https://pubmed.ncbi.nlm.nih.gov/28714979/)
57. C. Voigt *et al.*, Cancer cells induce interleukin-22 production from memory CD4<sup>+</sup> T cells via interleukin-1 to promote tumor growth. *Proc. Natl. Acad. Sci. U.S.A.* **114**, 12994–12999 (2017). doi: [10.1073/pnas.1705165114](https://doi.org/10.1073/pnas.1705165114); pmid: [29150554](https://pubmed.ncbi.nlm.nih.gov/29150554/)
58. T. L. Denning, G. Kim, M. Kronenberg, Cutting edge: CD4+CD25+ regulatory T cells impaired for intestinal homing can prevent colitis. *J. Immunol.* **174**, 7487–7491 (2005). doi: [10.4049/jimmunol.174.12.7487](https://doi.org/10.4049/jimmunol.174.12.7487); pmid: [15944246](https://pubmed.ncbi.nlm.nih.gov/15944246/)
59. D. Dangaj *et al.*, Cooperation between constitutive and inducible chemokines enables T cell engraftment and immune attack in solid tumors. *Cancer Cell* **35**, 885–900.e10 (2019). doi: [10.1016/j.ccell.2019.05.004](https://doi.org/10.1016/j.ccell.2019.05.004); pmid: [31185212](https://pubmed.ncbi.nlm.nih.gov/31185212/)
60. A. González-Martín, L. Gómez, J. Lustgarten, E. Mira, S. Mañes, Maximal T cell-mediated antitumor responses rely upon CCR5 expression in both CD4(+) and CD8(+) T cells. *Cancer Res.* **71**, 5455–5466 (2011). doi: [10.1158/0008-5472.CAN-11-1687](https://doi.org/10.1158/0008-5472.CAN-11-1687); pmid: [21715565](https://pubmed.ncbi.nlm.nih.gov/21715565/)
61. A. M. Cooper, IL-17 and anti-bacterial immunity: Protection versus tissue damage. *Eur. J. Immunol.* **39**, 649–652 (2009). doi: [10.1002/eji.200839090](https://doi.org/10.1002/eji.200839090); pmid: [19283706](https://pubmed.ncbi.nlm.nih.gov/19283706/)
62. T. Yokoo *et al.*, Liver-targeted hydrodynamic gene therapy: Recent advances in the technique. *World J. Gastroenterol.* **22**, 8862–8868 (2016). doi: [10.3748/wjg.v22.i40.8862](https://doi.org/10.3748/wjg.v22.i40.8862); pmid: [27833377](https://pubmed.ncbi.nlm.nih.gov/27833377/)
63. A. K. Holmer *et al.*, Biomarkers are associated with clinical and endoscopic outcomes with vedolizumab treatment in Crohn's disease. *Therap. Adv. Gastroenterol.* **13**, 1756284820971214 (2020). doi: [10.1177/1756284820971214](https://doi.org/10.1177/1756284820971214); pmid: [33240396](https://pubmed.ncbi.nlm.nih.gov/33240396/)
64. J. Lecuelle *et al.*, MER4 endogenous retrovirus correlated with better efficacy of anti-PD1/PD-L1 therapy in non-small cell lung cancer. *J. Immunother. Cancer* **10**, e004241 (2022). doi: [10.1136/jitc-2021-004241](https://doi.org/10.1136/jitc-2021-004241); pmid: [35277462](https://pubmed.ncbi.nlm.nih.gov/35277462/)
65. L. Albiges *et al.*, Safety and efficacy of nivolumab in metastatic renal cell carcinoma (mRCC): Final analysis from the NIVOREN GETUG AFU 26 study. *J. Clin. Oncol.* **37** (7\_suppl), 542 (2019). doi: [10.1200/JCO.2019.37.7\\_suppl.542](https://doi.org/10.1200/JCO.2019.37.7_suppl.542)
66. G. P. Sonpavde *et al.*, Primary results of STRONG: An open-label, multicenter, phase 3b study of fixed-dose durvalumab monotherapy in previously treated patients with urinary tract carcinoma. *Eur. J. Cancer* **163**, 55–65 (2022). doi: [10.1016/j.ejca.2021.12.012](https://doi.org/10.1016/j.ejca.2021.12.012); pmid: [35042068](https://pubmed.ncbi.nlm.nih.gov/35042068/)
67. A. Liesz *et al.*, Regulatory T cells are key cerebroprotective immunomodulators in acute experimental stroke. *Nat. Med.* **15**, 192–199 (2009). doi: [10.1038/nm.1927](https://doi.org/10.1038/nm.1927); pmid: [19169263](https://pubmed.ncbi.nlm.nih.gov/19169263/)
68. C. Benakis *et al.*, Commensal microbiota affects ischemic stroke outcome by regulating intestinal  $\gamma\delta$  T cells. *Nat. Med.* **22**, 516–523 (2016). doi: [10.1038/nm.4068](https://doi.org/10.1038/nm.4068); pmid: [27019327](https://pubmed.ncbi.nlm.nih.gov/27019327/)
69. R. J. Miraglia *et al.*, Single-cell transcriptomics of regulatory T cells reveals trajectories of tissue adaptation. *Immunity* **50**, 493–504.e7 (2019). doi: [10.1016/j.immuni.2019.01.001](https://doi.org/10.1016/j.immuni.2019.01.001); pmid: [30737144](https://pubmed.ncbi.nlm.nih.gov/30737144/)
70. A. R. Muñoz-Rojas, D. Mathis, Tissue regulatory T cells: Regulatory chameleons. *Nat. Rev. Immunol.* **21**, 597–611 (2021). doi: [10.1038/s41577-021-00519-w](https://doi.org/10.1038/s41577-021-00519-w); pmid: [33772242](https://pubmed.ncbi.nlm.nih.gov/33772242/)
71. N. Yosef *et al.*, Dynamic regulatory network controlling TH17 cell differentiation. *Nature* **496**, 461–468 (2013). doi: [10.1038/nature11981](https://doi.org/10.1038/nature11981); pmid: [23467089](https://pubmed.ncbi.nlm.nih.gov/23467089/)
72. U. U. Uche *et al.*, PIK3IP1/TrIP restricts activation of T cells through inhibition of PI3K/Akt. *J. Exp. Med.* **215**, 3165–3179 (2018). doi: [10.1084/jem.20172018](https://doi.org/10.1084/jem.20172018); pmid: [30429249](https://pubmed.ncbi.nlm.nih.gov/30429249/)
73. A. Fischer *et al.*, Differential effects of  $\alpha$ 4 $\beta$ 7 and GPR15 on homing of effector and regulatory T cells from patients with UC to the inflamed gut in vivo. *Gut* **65**, 1642–1664 (2016). doi: [10.1136/gutjnl-2015-310022](https://doi.org/10.1136/gutjnl-2015-310022); pmid: [26209553](https://pubmed.ncbi.nlm.nih.gov/26209553/)
74. G. D'Haens *et al.*, Effect of PF-00547659 on central nervous system immune surveillance and circulating  $\beta$ 7+ T cells in Crohn's disease: Report of the TOSCA study. *J. Crohns Colitis* **12**, 188–196 (2018). doi: [10.1093/ecco-jcc/jjx128](https://doi.org/10.1093/ecco-jcc/jjx128); pmid: [28961770](https://pubmed.ncbi.nlm.nih.gov/28961770/)
75. G. Calenda *et al.*, Integrin  $\alpha$ 4 $\beta$ 7 blockade preferentially impacts CCR6+ lymphocyte subsets in blood and mucosal tissues of naive Rhesus macaques. *J. Immunol.* **200**, 810–820 (2018). doi: [10.4049/jimmunol.1701150](https://doi.org/10.4049/jimmunol.1701150); pmid: [29196458](https://pubmed.ncbi.nlm.nih.gov/29196458/)
76. M. I. Love, W. Huber, S. Anders, Moderated estimation of fold change and dispersion for RNA-seq data with DESeq2. *Genome Biol.* **15**, 550 (2014). doi: [10.1186/s13059-014-0550-8](https://doi.org/10.1186/s13059-014-0550-8); pmid: [25516281](https://pubmed.ncbi.nlm.nih.gov/25516281/)
77. M. E. Ritchie *et al.*, limma powers differential expression analyses for RNA-sequencing and microarray studies. *Nucleic Acids Res.* **43**, e47 (2015). doi: [10.1093/nar/gkv007](https://doi.org/10.1093/nar/gkv007); pmid: [25605792](https://pubmed.ncbi.nlm.nih.gov/25605792/)
78. H. Lin, S. D. Peddada, Analysis of compositions of microbiomes with bias correction. *Nat. Commun.* **11**, 3514 (2020). doi: [10.1038/s41467-020-17041-7](https://doi.org/10.1038/s41467-020-17041-7); pmid: [32665548](https://pubmed.ncbi.nlm.nih.gov/32665548/)
79. H. Mallick *et al.*, Multivariable association discovery in population-scale meta-omics studies. *PLOS Comput. Biol.* **17**, e1009442 (2021). doi: [10.1371/journal.pcbi.1009442](https://doi.org/10.1371/journal.pcbi.1009442); pmid: [34784344](https://pubmed.ncbi.nlm.nih.gov/34784344/)
80. N. Segata *et al.*, Metagenomic biomarker discovery and explanation. *Genome Biol.* **12**, R60 (2011). doi: [10.1186/gb-2011-12-r60](https://doi.org/10.1186/gb-2011-12-r60); pmid: [21702898](https://pubmed.ncbi.nlm.nih.gov/21702898/)
81. P. Bankhead *et al.*, QuPath: Open source software for digital pathology image analysis. *Sci. Rep.* **7**, 16878 (2017). doi: [10.1038/s41598-017-17204-5](https://doi.org/10.1038/s41598-017-17204-5); pmid: [29203879](https://pubmed.ncbi.nlm.nih.gov/29203879/)
82. C. Grajeda-Iglesias *et al.*, Oral administration of *Akkermansia muciniphila* elevates systemic antiaging and anticancer metabolites. *Aging (Albany NY)* **13**, 6375–6405 (2021). doi: [10.18632/aging.202739](https://doi.org/10.18632/aging.202739); pmid: [33653967](https://pubmed.ncbi.nlm.nih.gov/33653967/)
83. S. Durand, C. Grajeda-Iglesias, F. Aprahamian, N. Nirmalathasan, O. Kepp, G. Kroemer, "The intracellular metabolome of starving cells," in *Methods in Cell Biology*, O. Kepp, L. Galluzzi, Eds. (Academic, 2021), vol. 164 of *Monitoring Vesicular Trafficking in Cellular Responses to Stress - Part A*, pp. 137–156; <https://www.sciencedirect.com/science/article/pii/S0091679X21000431>.

## ACKNOWLEDGMENTS

We would like to particularly thank the animal facility and the Flow Cytometry and Pathology Platforms of Gustave Roussy, especially P. Gonin, L. Touchard, C. Metereau, A. Noel, and O. Bawa, and the PREMIS operational team, especially S. Farhane (project leader), S. Messayke (pharmacovigilance), L. Bedouda (clinical research associate), R. Chaabane (clinical research associate), C. Mohamed-Djalil (clinical research associate), and all investigators. Some figure items were partly generated using Servier Medical Art, provided by Servier, licensed under a Creative Commons Attribution 3.0 unported license. **Funding:** This work was supported by the SEERAVE Foundation, European Union Horizon 2020, Project Number 825410 and Project Acronym ONCOBIOHME, Institut National du Cancer (INCA), ANR Ileobiome – 19-CE15-0029-01, ANR RHU5 ANR-21-RHUS-0017 IMMUNOLIFE, AdCAM INCA\_16698, ANR-IHU Méditerranée-Infections, Ligue contre le cancer, LABEX Oncolmmunology, la direction generale de l'offre de soins (DGOS), SIRIC SOCRATE (INCA/DGOS/INSERM 6043), and PACRI network. G.K. was supported by the Ligue contre le Cancer (équipe labellisée); Agence Nationale de la Recherche (ANR) – Projets blancs; AMMICA US23/CNRS UMS3655; Cancéropôle Ile-de-France; Fondation pour la Recherche Médicale (FRM); Equipex Onco-Pheno-Screen; European Joint Programme on Rare Diseases (EJPRD); European Research Council (ICD-Cancer), European Union Horizon 2020 program Crimson; Institut National du Cancer (INCA); Institut Universitaire de France; LabEx Immuno-Oncology (ANR-18-IDEX-0001); a Cancer Research ASPIRE Award from the Mark Foundation; SIRIC Stratified Oncology Cell DNA Repair and Tumor Immune Elimination (SOCRATE); SIRIC Cancer Research and Personalized Medicine (CARPEM); the Prism project funded by the Agence Nationale de la Recherche under grant number ANR-18-IBHU-0002; and the TriPoD European Research Council Advanced EU (322856) and Recherche Hospitalo-Universitaire iMAP (ANR-16-RHUS-0001) grants to D.K. O.K. was funded by INCA and the DIM Elicit. The PREMIS study was funded by Gustave Roussy fondation & Malakoff

Humanis. The Bladder cohort from IOPREDI ancillary study / STRONG study (NCT03084471) was funded by AstraZeneca. This study contributes to the IdEx Université de Paris ANR-18-IDEX-0001. M.F. was funded by SEERAVE Foundation. C.Ra. received a fellowship from Immuntrain within the Marie-Slodowska Curie Training network of the European Union (LMU Klinikum). L.D., B.R., S.Y., and F.X.D. were supported by Philantropia at Gustave Roussy Foundation. I.La. was funded by Fondation pour la Recherche Médicale (FRM). A.Sc. and N.W. were funded by DFG (German Research Foundation) – Project-ID 403324012 – SFB 1382. **Author contributions:** Conceptualization: L.Zi., G.K., C.Ra., M.F.; Data curation: I.La., K.M., G.V., V.M., A.M.T.; Formal analysis: M.F., C.Ra., C.A.C.S., I.La., C.D., M.L., S.D., K.M., S.Y., J.E.F., C.Ri., L.L., G.V., E.L.C., R.D., V.M., D.D., A.M.T., L.D.; Funding acquisition: L.Zi., G.K., L.D.; Investigation: M.F., C.Ra., C.A.C.S., A.L.T., I.La., A.L.M.L.V., L.Zh., C.Th., I.Le., M.M., E.P., R.B., M.D.M.F., S.Z., A.R., M.L., G.F., P.L., A.Si., K.M., C.A.D., M.P.R., M.T.A., J.C., J.B., L.L., R.D., C.Tr., N.C., V.M., L.D., G.K., L.Zi.; Methodology: M.F., C.Ra., A.L.T., I.La., L.Zh., I.Le., A.Si., F.Gi., S.Y., O.K., A.Sc., N.W., J.S.G., S.K., J.B., L.L., N.Ga., B.Q., E.L.C., L.B., J.P.G., R.D., C.Tr., F.Gh., V.M., D.K., A.M.T., N.S., G.K., L.Zi.; Resources: A.Si., K.M., C.A.D., F.Gi., M.P.R., S.T., A.Sc., N.W., J.S.G., S.K., E.L.C., L.B., J.P.G., A.J., N.Ge., E.G., N.L., R.K., R.D., B.B., C.Tr., F.Gh., N.C., V.M., D.K., L.A., A.M.T., N.S., F.X.D., A.M., B.R., L.D., G.K., L.Zi.; Software: M.F., I.La., C.D., K.M., C.Ri., G.V., V.M., D.D., A.M.T.; Supervision: L.Zi., G.K., M.F., C.Ra., L.D., F.Gi., O.K., E.L.C., N.L., D.K., N.S.; Validation: M.F., C.Ra., C.A.C.S., L.D.; Visualization: M.F., C.Ra., C.A.C.S., A.L.T., I.La., A.L.M.L.V., R.B., L.D.; Writing – original draft: L.Zi., G.K., C.Ra., M.F.; Writing – review & editing: L.Zi., G.K., C.Ra., M.F., C.A.C.S., D.D., A.L.T., M.P.R., O.K., E.G., N.L., V.M., L.D.

**Competing interests:** L.Zi. founded and is the SAB president of everImmune. L.Zi. had grant support from Daichi Sankyo, Kaleido, 9 m, and Pileje. G.K. holds research contracts with Daichi Sankyo, Eleor, Kaleido, Lytx Pharma, PharmaMar, Osasuna Therapeutics, Samsara Therapeutics, Sanofi, Tollis, and Vascage. G.K. has consulted for Reithera. G.K. is on the board of directors of the Bristol Myers Squibb Foundation France. G.K. is a scientific cofounder of everImmune, Osasuna Therapeutics, Samsara Therapeutics, and Therastab Bio. G.K. is in the scientific advisory boards of Hevolution, Institut Servier, and Longevity Vision Funds. G.K. is the inventor of patents covering therapeutic targeting of aging, cancer, cystic fibrosis, and metabolic disorders. Among these, patents were licensed to Bayer (WO2014020041-A1, WO2014020043-A1), Bristol-Myers Squibb (WO2008057863-A1), Osasuna Therapeutics (WO2019057742-A1), PharmaMar (WO2022049270A1 and WO2022048775-A1), Raptor Pharmaceuticals (EP2664326-A1), Samsara Therapeutics (GB202017553D0), and Therastab Bio (EP3684471A1). R.D. filed the WO2022/268841 A1 patent. O.K. is a scientific cofounder of Samsara Therapeutics. L.D. is member of the SAB of everImmune. I.La. is an advisor or consultant for Astellas, BMS, Ipsen, Janssen, MSD, Pfizer, Eisai, and Roche. Gustave Roussy filed a patent with registration number EP21305846.4 and reference number B210162EPA/VEM/CPO, "Methods for diagnosing a cancer-induced ileopathy and their use for improving cancer treatment by immunotherapy" licensed to everImmune. The remaining authors declare no competing interests. **Data and materials availability:** All data are available in the main text or the supplementary materials. Patient data are available to vetted researchers and not to the broader public through a data transfer agreement. A materials transfer agreement will be necessary to access to intestinal species from everImmune or Gustave Roussy. Bulk RNA-Seq data (E-MTAB-12787), single-cell Rhapsody RNA-Seq data (E-MTAB-12812), 16S rRNA sequencing data (E-MTAB-12846), 10X single-cell RNA and TCR sequencing data (E-MTAB-12846), metagenomics data (bioprojects PRJNA944152 and PRJNA751792), and metabolomics data (Elsevier/Mendeley data DOI: [10.17632/4b76mz87r6.1](https://doi.org/10.17632/4b76mz87r6.1)) are all publicly available. **License information:** Copyright © 2023 the authors, some rights reserved; exclusive licensee American Association for the Advancement of Science. No claim to original US government works. <https://www.science.org/about/science-licenses-journal-article-reuse>

## SUPPLEMENTARY MATERIALS

[science.org/doi/10.1126/science.aba2296](https://science.org/doi/10.1126/science.aba2296)

Figs. S1 to S10

Tables S1 to S9

Data S1 and S2

MDAR Reproducibility Checklist

[View/request a protocol for this paper from Bio-protocol.](#)

Submitted 21 January 2022; resubmitted 12 December 2022

Accepted 14 April 2023

10.1126/science.aba2296

## A microbiota-modulated checkpoint directs immunosuppressive intestinal T cells into cancers

Marine Fidelle, Conrad Rauber, Carolina Alves Costa Silva, Ai-Ling Tian, Imran Lahmar, Anne-Laure Mallard de La Varende, Liwei Zhao, Cassandra Thelemaque, Isabelle Lebhar, Meriem Messaoudene, Eugénie Pizzato, Roxanne Birebent, Maxime Descartes Mbogning Fonkou, Silvia Zoppi, Anna Reni, Cécile Dalban, Marion Leduc, Gladys Ferrere, Sylvère Durand, Pierre Ly, Aymeric Silvin, Kevin Mulder, Charles-Antoine Dutertre, Florent Ginhoux, Satoru Yonekura, Maria Paula Roberti, Maryam Tidjani-Alou, Safae Terrisse, Jianzhou Chen, Oliver Kepp, Angela Schippers, Norbert Wagner, Javier Suárez-Gosálvez, Sebastian Kobold, Jean-Eudes Fahrner, Corentin Richard, Jacques Bosq, Leonardo Lordello, Giacomo Vitali, Nathalie Galleron, Benoît Quinquis, Emmanuelle Le Chatelier, Lucas Blanchard, Jean-Philippe Girard, Anne Jarry, Nadine Gervois, Emmanuelle Godefroy, Nathalie Labarrière, Ronald Koschny, Romain Daillère, Benjamin Besse, Caroline Truntzer, François Ghiringhelli, Nicolas Coatnoan, Vanessa Mhanna, David Klatzmann, Damien Drubay, Laurence Albiges, Andrew Maltez Thomas, Nicola Segata, François-Xavier Danlos, Aurélien Marabelle, Bertrand Routy, Lisa Derosa, Guido Kroemer, and Laurence Zitvogel

*Science* **380** (6649), eabo2296. DOI: 10.1126/science.abo2296

### Editor's summary

Immune checkpoint blockade therapy for the treatment of cancer can have reduced efficacy when antibiotics are administered and then discontinued before the start of therapy. Fidelle *et al.* investigated whether bacteria that rebound may affect the treatment response (see the Perspective by Pratt and Milner). *Enterocloster* species that recolonized the guts of mice treated with antibiotics down-regulated the expression of MAdCAM-1, the ligand for integrin  $\alpha 4\beta 7$  that helps to retain an immunosuppressive subset of T cells (Tr17 cells) within the gut. This leads to transit of Tr17 cells to tumors and tumor-draining lymph nodes, where they compromise immune checkpoint blockade therapy. In cancer patients undergoing immunotherapy, low levels of serum-soluble MAdCAM-1 correlated with intestinal dysbiosis and poor clinical outcomes for renal, bladder, and lung tumors. —Priscilla N. Kelly & Seth Thomas Scanlon

### View the article online

<https://www.science.org/doi/10.1126/science.abo2296>

### Permissions

<https://www.science.org/help/reprints-and-permissions>

Use of this article is subject to the [Terms of service](#)

*Science* (ISSN 1095-9203) is published by the American Association for the Advancement of Science. 1200 New York Avenue NW, Washington, DC 20005. The title *Science* is a registered trademark of AAAS.

Copyright © 2023 The Authors, some rights reserved; exclusive licensee American Association for the Advancement of Science. No claim to original U.S. Government Works